OPTO-ELECTRONIC CLASS AB MICROWAVE POWER AMPLIFIER USING PHOTOCONDUCVIVE SWITCH TECHNOLOGY

A Dissertation
presented to
the Faculty of the Graduate School
University of Missouri-Columbia

In Partial Fulfillment
of the Requirement for the Degree

Doctor of Philosophy

---

by
CHIH-JUNG HUANG

Dr. Robert M. O'Connell, Dissertation Supervisor

AUGUST 2006

The undersigned, appointed by the Dean of the Graduate School, have examined the dissertation entitled

OPTO-ELECTRONIC CLASS AB MICROWAVE POWER AMPLIFIER USING PHOTOCONDUCVIVE SWITCH TECHNOLOGY

Presented by Chih-Jung Huang

A candidate for the degree of Doctor of Philosophy
And hereby certify that their opinion it is worthy of acceptance.

_____
Robert O'Connell, Ph.D.

_____
William Nunnally, Ph.D.

_____
Naz Islam, Ph.D.

_____
Justin Legarsky, Ph.D.

_____
H. R. Chandrasekhar, Ph.D.

ACKNOWLEDGEMENTS

This dissertation as well as the entire Ph.D. process would not have been possible without the help of many people.

First, I would like to thank my advisor, Dr. Robert M. O'Connell for his advice, guidance, and encouragement during this research. Furthermore, thanks are extended to all of my committee members, Dr. William Nunnally, Dr. Naz Islam, Dr. Justin Legarsky and Dr. H. R. Chandrasekhar, for their review of the manuscript and valuable comments along the way.

Secondly, I want to dedicate this dissertation to all my beloved family members who have provided support during this entire process from thousands miles away in Taiwan. Thank you for being part of it.

TABLE OF CONTENTS

LIST OF TABLES

LIST OF FIGURES

OPTO-ELECTRONIC CLASS AB MICROWAVE POWER AMPLIFIER USING PHOTOCONDUCVIVE SWITCH TECHNOLOGY

Chih-Jung Huang

Dr. Robert M. O'Connell, Dissertation Supervisor

ABSTRACT

Next generation land-based, mobile, phased-array radar systems for battlefield applications must meet constraints on volume, weight, power consumption, and data processing capability that are currently not available. The most inefficient component in a phased array radar system is the final power amplifier in each transmit-receive (TR) module. More recent final power amplifiers for TR modules have been configured in the Class AB or push-pull mode with a theoretical efficiency of 78.5% and an operational efficiency of only 20% at x-band (8-12.5 GHz) frequency. Note that an efficiency of 10% requires ten times the radiated power to be generated and 90% of the delivered energy to be removed as heat. In this dissertation, we present a new scheme of power amplifier, in particular, an opto-electronic (OE) Class AB push-pull microwave power amplifier. With this amplifier, 50.0 % of circuit efficiency and 2.2 Watts of output power can be achieved at X-band (8-12.5 GHz) by utilizing a novel photoconductive semiconductor switch (PCSS) based on intrinsic GaAs instead of the traditional microwave transistors.

Chapter 1 Introduction

1.1 General description

With the developments in wireless systems, data communications, telecommunications, and aerospace systems, the demand for improved microwave communication capability has been continually increasing over the last decade. For applications such as radar, scientists are trying to improve the state-of-the-art in system architectures and to produce more compact and lighter systems with reduced power requirements [1]. To achieve this goal, avoiding unnecessary power losses in order to reduce the size of the heat sinks is an important issue.

Fig. 1.1 shows the block diagrams of a typical wireless transmitter and receiver module [2]. The first stage of the transmitter is the modulator that is used to modulate the baseband signal into an intermediate frequency. This intermediate frequency (IF) signal is then shifted up in frequency to the desired RF frequency using a mixer. The mixer operates by producing the sum and difference of the input IF signal frequency and the frequency of a separate local oscillator (LO). In order to allow the sum frequency to pass, while rejecting the much lower difference frequency, a bandpass filter (BPF) is utilized. A power amplifier (PA) is used to increase the output power of the transmitter. Finally, this baseband information is placed onto a high frequency sine wave carrier signal that can be radiated by the antenna using a propagating electromagnetic plane wave. The receiver of Fig. 1.1 can recover the transmitted baseband data by essentially reversing the functions of the transmitter components.

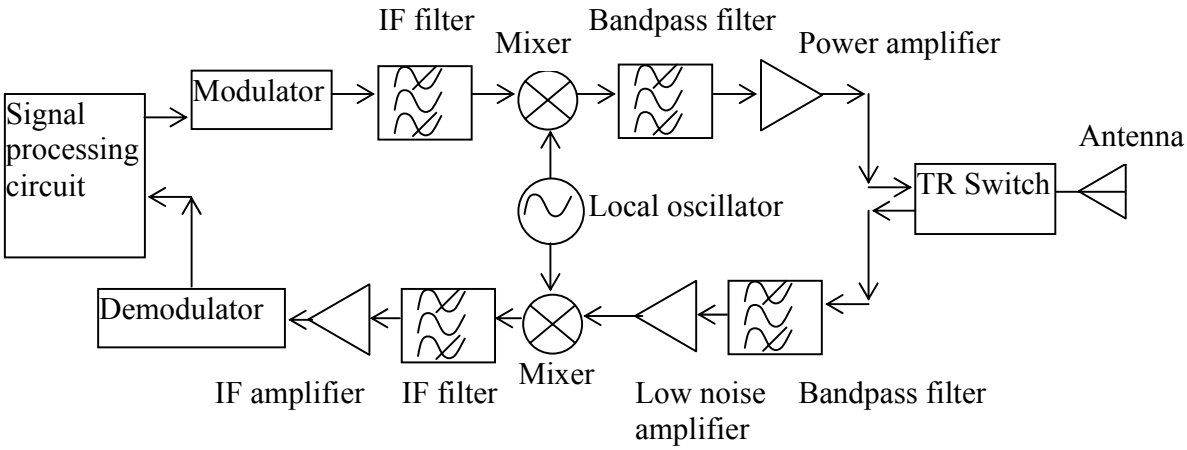

Fig. 1.1 Block diagram of a typical wireless transmitter and receiver module.

In microwave communications, including phased array radar systems, the major source of inefficiency is the amplifier circuits in the transmit-receive or TR modules, especially the power amplifier (PA), which is usually required in the final stage of the transmitter module. The purpose of the PA in the module is to provide sufficient gain and output power to meet the radar system output requirements. Typical output powers may be on the order of 0.3 to 0.6 W for a handheld cellular phone, or in the range of 10 to 100 W for a base station transmitter. Other important parameters of the PAs are linearity and operating frequency.

The capability of a PA depends highly on the performance of the microwave transistors selected. In order to achieve high power output capability, the microwave transistors need to have high breakdown voltage. Also, high operation frequency for the microwave transistors is necessary because most modern wireless systems rely on RF or microwave signals, usually in the UHF (100 MHz) to millimeter wave (30 GHz) frequency range. RF or microwave signals offer wide bandwidths, and are able to

penetrate fog, dust, foliage, and even buildings and vehicles. Most of the microwave transistors in use today are three terminal electrically controlled solid state devices such as field effect transistors (FETs), hetrojunction bipolar transistors (HBTs), and high electron mobility transistors (HEMTs) [2]. All these devices can be fabricated in semiconductor materials such as Silicon (Si) and Gallium Arsenide (GaAs). Moreover, microwave transistor PAs are characterized by low cost, they are reliable, and they can be easily integrated in monolithic integrated circuits with other system components such as mixers and oscillators.

In this dissertation, we present a new scheme of PA, in particular, an opto-electronic (OE) Class AB push-pull microwave power amplifier. With this amplifier, high circuit efficiency and reasonable output power can be achieved at X-band (8-12.5 GHz) by utilizing a novel photoconductive semiconductor switch (PCSS) based on intrinsic GaAs instead of the traditional electrically controlled microwave transistors. The objective of this project is to investigate and develop the new PA with an ultimate goal of an efficiency of 60% at 10 GHz.

1.2 Chapter summary

The remainder of this dissertation contains four chapters. Chapter 2 is the literature review. It describes previous related work by other researchers. Included is a review of work on PCSSs and PAs that have relevance to our research. We will also describe the state-of-the-art and the limitations of PCSSs and PAs today. Chapter 3 describes our research approach. It includes an analytical description of the semi-

insulating (SI) and intrinsic GaAs microwave PCSS and the OE Class AB push-pull PA and a discussion of methods used in overcoming previous limitations. In addition, in order to increase the output power capability at 10 GHz, a series and a multi-layer PCSS structure will be described.

Chapter 4 contains our simulation results. It describes the software used for simulation, and describes and analyzes the simulation results and compares them with analytical results. Finally, Chapter 5 concludes the dissertation and also defines continuation work that might be done in the future.

Chapter 2 Literature Review

We will divide this chapter into three sections. In the first section, we will discuss different classes of power amplifiers and their limitations. In the second section, we will explain why our OE Class AB push-pull PA promises to be better than others in some specific ways at 10 GHz frequency. In the third section, we will review different photoconductive semiconductor switches (PCSSs) and their applications.

2.1 Power amplifiers

Power amplifiers (PAs) are circuits for converting dc-input power into significant amounts of RF or microwave output power. In most cases, PAs are not just small signal amplifiers driven into saturation. There exists a great variety of PAs, and most employ techniques beyond simple linear amplification [3]. According to the relations between input and output RF microwave waveforms of the power amplifiers, we can divide them into linear and nonlinear amplifiers. Class A, B and AB are linear power amplifiers, and Class C, D, and E are nonlinear power amplifiers [4,5].

The Class A PA, shown in Fig. 2.1, has the best linearity among all PAs since the Q (quiescent) point is selected to keep the transistor in its active region. Linearity is a measure of the extent to which the output amplified waveform is identical in shape to that of the input RF waveform. The RF choke (RFC) in Fig. 2.1 provides a constant DC input current. The ideal collector-voltage and collector-current waveforms are sinusoids. The Class A PA offers high gain, high linearity, and operation close to the maximum

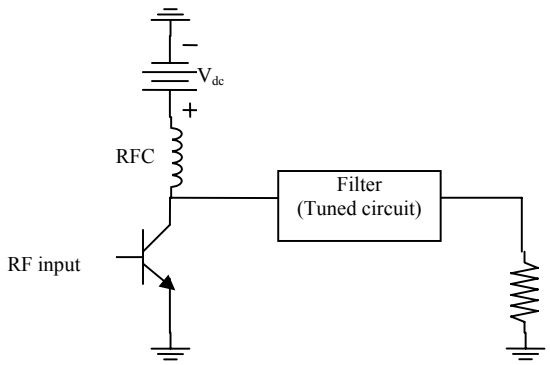

Fig. 2.1 Class A power amplifier

operating frequency of the transistor. Here, gain can be defined as the average output power divided by the input microwave average power.

$$G = P_L / P_{mic} \qquad (2.1)$$

However, the theoretical efficiency of the Class A PA, defined as the average output microwave power divided by the average DC input power, is very low, only 25% [4]; in fact, previous systems initially employed Class A PAs with operating efficiency of only 10-12% at S-band [1] and above [6], a big disadvantage for our purposes.

The Class B or AB PA is also called a push-pull PA. A simple push-pull PA is shown in Fig. 2.2 [7]. Note that it contains both NPN and PNP transistors. The gate bias in an ideal push-pull PA is set at the threshold of conduction; therefore, each transistor is active half of the time and its collector current is a half sinusoid. The push-pull PA also provides good linear amplification because the output current is proportional to the gate drive amplitude. However, the transconductance of the n-type transistor is an order of magnitude greater than that of the p-type transistor due to the difference between electron and hole mobilities, which limits the operating gain and efficiency of the push-pull pair.

Therefore, an improved push-pull PA, shown in Fig. 2.3, was developed, which requires only n-type transistors [8,9]. Recently, the integrated-antenna concept was applied to push-pull PA [10-14]. In this approach, the antenna serves as an out of phase power combiner and tuned load for higher harmonics; thus, the output transformer or balun is not required, which reduces power losses and increases circuit efficiency. A power added efficiency (PAE) of 50 % has been demonstrated at an operating frequency of 3 GHz. However, at 5 GHz, the PAE drops to only 32 %. For microwave systems, the power added efficiency (PAE) can be defined as

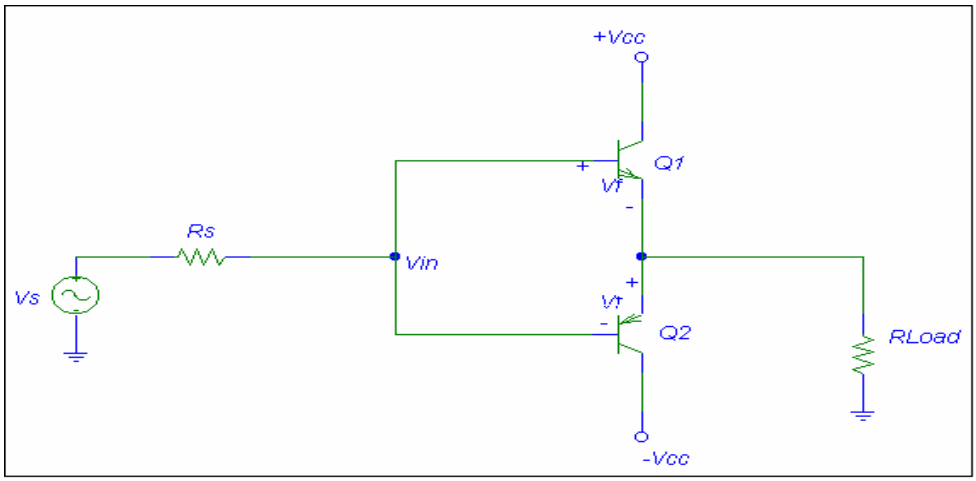

Fig. 2.2 Push-pull power amplifier

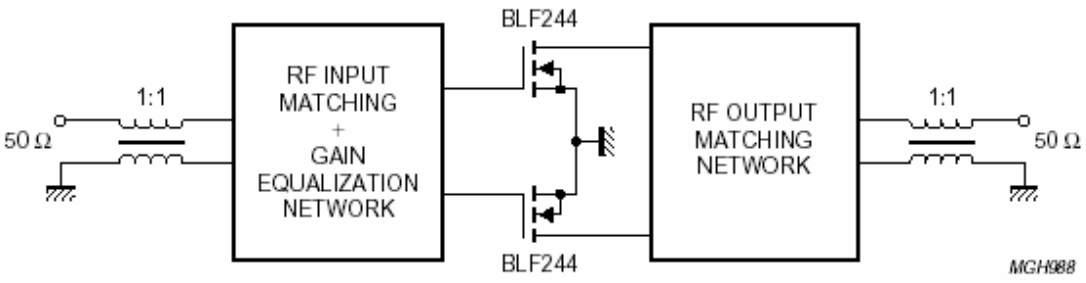

Fig. 2.3 Improved push-pull power amplifier using transformers or baluns.

$$PAE = (P_L - P_{mic}) / P_s \qquad (2.2)$$

where P_s is the average input DC power, P_{mic} is the average input microwave power, and P_L is the average output power.) This loss in PAE is due to the limitations of the transformer or balun. For the linear amplifiers, the Class AB PA shows better theoretical efficiency, 78.5 %, than the class A PA, 25%.

Many applications do not require linear RF amplification and can therefore make use of the greater efficiency offered by nonlinear Class C tuned power amplifiers [4]. The circuit topology of the classical Class C PA is the same as that of the Class A PA, illustrated in Fig. 2.1. The active device is also driven to act as a current source. However, the current waveform it produces is not the sinusoidal current desired in the load because the gate of the Class C PA is biased below threshold, so that the transistor is active less than half of the RF cycle. Thus, linearity is lost and a tuned output circuit (tank circuit) or filter is needed in order to produce a sinusoidal signal at the load. The theoretical efficiency of an ideal Class C PA is 100 %, and systems operating with PAE of 50 % at 900 MHz have been demonstrated [15,16].

The Class D PA is also a nonlinear PA, which is very similar to the Class B and Class AB PAs, shown in Fig. 2.2. The biggest difference is that the two transistors here act as switches. A Class D amplifier employs a pair of active devices and a tuned output circuit (tank circuit), which is not needed in the Class AB PA. The devices are driven to act as a two-pole switch that defines either a rectangular voltage or rectangular current waveform. The output circuit is tuned to the switching frequency and filters its harmonics, resulting in a sinusoidal output. The efficiency of an ideal Class D PA is 100 %. However, because of switching, conduction, and gate drive losses of the transistors,

an efficiency of 90 % has been observed at only 14 MHz [17,18] and only 75 % at 900 MHz [19,20]. Again, the transformer or balun limits the Class D PA for use at high frequency operation.

Similar to the Class C and D amplifiers, the Class E PA is another nonlinear PA. The circuit setup for the Class E PA is similar to that of the Class A amplifier shown in Fig. 2.1, but unlike the Class A PA, the transistor in the Class E PA is driven by a rectangular input pulse [5]. Therefore, an output tank or tuned circuit is needed to filter unwanted harmonics. In the ideal Class E PA, the collector voltage drops to zero and has zero slope just as the transistor turns on, resulting in an ideal efficiency of 100 %. However, the transistor switching losses reduce the circuit efficiency. Class E PAs have been demonstrated with better PAE than other classes of PAs at different frequencies [21].

2.2 Opto-electronic (OE) Class AB push-pull microwave power amplifier at 10 GHz (X band).

In wireless transmitter and receiver systems, size and efficiency are important factors. In order to accomplish high circuit overall efficiency and power added efficiency (PAE), a new scheme of PA, called an opto-electronic (OE) Class AB push-pull microwave power amplifier, shown in Fig. 2.4, is proposed.

In this new scheme, optical input is used instead of electrical input, which leads to several advantages of the system, the first of which is optical isolation of the input control circuit from the main circuit. Switch control from a completely isolated source offers multiple potential system benefits. Control source isolation and the ability to position the

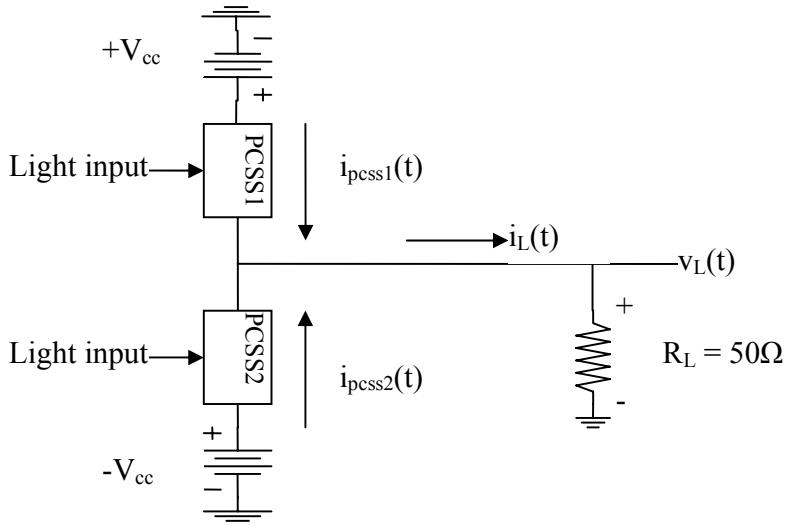

Fig. 2.4 Opto-electronic (OE) Class AB push-pull microwave power amplifier.

controlling light beam will permit many sources to be applied to a single load or a single source to be applied to multiple loads. Another advantage of using optical input is that by using two optically controlled photoconductive semiconductor switches (PCSSs), which are polarity independent, we eliminate the polarity issue described above. Thus, higher efficiency should be achievable. Improving the efficiency will reduce the power and thermal management requirements, which translate directly to the weight and volume of the system. A third advantage is that, with optical illumination, an input matching network, which is required when using an electrical RF input signal, is not necessary.

Class E PAs have been shown to have better PAE than Class AB (push-pull) PAs at 10 GHz. For example, around 60 % circuit efficiency has been achieved in a Class E PA at X band [22-24] versus only 20 % in a Class AB (push-pull) PA [25,26]. However, in this project, an OE Class AB push-pull PA was chosen over an OE Class E PA for two

reasons. The first reason is due to the simplicity of the input laser system. The input RF microwave signal to be carried by the CW light laser can be produced relatively easily by intensity modulating the light in the laser beam. This modulated light beam can be used in our OE Class AB push-pull microwave PA because it is a linear amplifier. In contrast, the Class E PA is a nonlinear amplifier which requires a rectangular light input pulse. It is more difficult to produce a rectangular light pulse than to intensity modulate the light. Therefore, the laser system is more complicated in the OE Class E PA. Secondly, due to the nonlinear nature of the Class E PA, a tank (tuned) circuit is necessary and needs to be well designed at the output stage of the amplifier in order to obtain a clean 10 GHz sinusoid output waveform. The trade off to these advantages is that the theoretical circuit efficiency for a Class AB PA is 78.5 % compared with the 100 % for the Class E PA.

2.3 Photoconductive semiconductor switches (PCSS)

In this section, electrically and optically controlled High Electron Mobility Transistors or HEMT devices will be discussed first. We will explain why this device is not suitable for our OE Class AB push-pull PA. Then, we will discuss photoconductive semiconductor switches, which are attractive for our PA.

2.3.1 Electrically and optically controlled HEMT devices

Recently, electrically controlled HEMT devices have been popular in monolithic microwave integrated circuits (MMICs) because of their high gain, low noise, and high

frequency response [27]. The HEMT is a heterostructure field effect device. The term "High Electron Mobility Transistor" is applied to the device because the structure takes advantage of the superior transport properties (high mobility and velocity) of electrons in a potential well within lightly doped semiconductor material such as GaAs. It is also called a Modulation Doped FET (MODFET).

Fig. 2.5 shows a cross-sectional view of a conventional HEMT device structure. Note that a wide bandgap semiconductor material (n-type AlGaAs) lies on an undoped narrow bandgap material (GaAs). AlGaAs and GaAs are the most common materials used for this structure. The thickness and doping density of the AlGaAs layer are chosen so that this layer is completely depleted of free electrons under normal operating conditions.

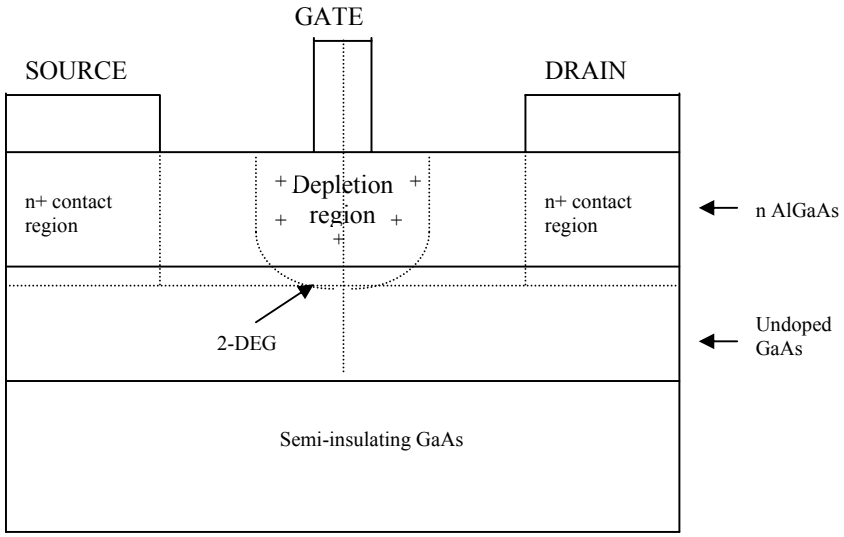

Fig. 2.5 A cross sectional view of a conventional HEMT device structure.

Fig. 2.6 shows the energy band diagram along the direction perpendicular to the heterojunction interface using the AlGaAs/GaAs interface, i.e., along the dotted line in Fig. 2.5. It shows that a sharp dip in the conduction band edge occurs in the HEMT at the AlGaAs/GaAs boundary. This results in a high carrier concentration in a narrow region along the GaAs side of the heterojunction. This high free-electron concentration is described as a two-dimensional electron gas (2-DEG). Electrons traveling in this region do not encounter ionized donor atoms because the GaAs is undoped. Therefore, ionized impurity scattering effects are absent, so that the electron mobility is high and the device has fast response time enabling high frequency operation [28].

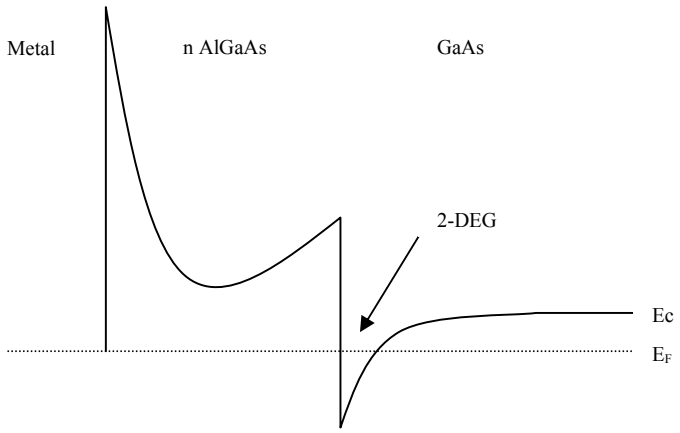

Fig. 2.6 Band diagram corresponding to the HEMT device structure of Fig. 2.5.

Various papers have described the characteristics of electrically controlled HEMTs with optical illumination to improve gain [29-33]. The results show the improvement of the device gain due to the photoconductive and photovoltaic effects. However, these electrically controlled HEMTs are not suitable for our OE Class AB push-pull PA design

because both p-type and n-type HEMT devices are still required. To eliminate this problem, a HEM photoconductive detector, often called a metal-semiconductor-metal photodetector, with a GaAs/AlGaAs/GaAs heterostructure, as shown in Fig. 2.7, was considered [34,35]. Both drain and source contacts are formed as Schottky contacts. When illuminated, electron and hole pairs generated in the GaAs layer exhibit an electric field between drain and source; the increased charge increases the conductivity in the 2-DEG layer. The response time, especially turn off time, depends on the thickness d of the GaAs. If d is small, short turn off time can be observed. However, the trade off is that the photogenerated current will be limited due to the absorption depth of GaAs. A turn

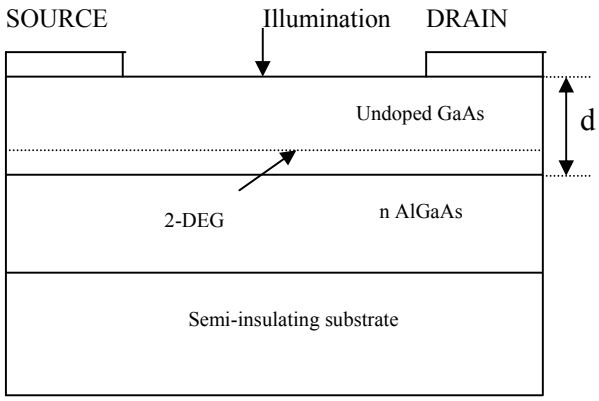

Fig. 2.7 A cross sectional view of a HEM photoconductive detector.

off or fall time of 22 ps has been achieved for d equal to 1 um as compared to 42 ps for d equal to 2 um [34,35]. The 1 um device is fast enough for 10 GHz operation, but the gain is too small because of the small value of d. The 2 um device is too slow. Thus, it was concluded that this device is not suitable for our PA and a different active switch was sought.

2.3.2 Photoconductive semiconductor switches (PCSSs)

Photoconductive semiconductor switches (PCSSs), as illustrated in Fig. 2.8, have been shown to offer several advantages over conventional gas, mechanical, and electrically triggered semiconductor switches. These include optical isolation of the trigger, very low relative jitter, very fast switching speeds, simple mechanical structure, extremely low inductance, and high thermal capacity [36-38]. Jitter of a conventional switching system results from jitter of the electrical systems generating the trigger pulses and from different switch closure times. The time delay between trigger pulse arrival and switch closure initiation depends upon the availability of a free electron. Faster electrical trigger pulse risetimes produce less jitter. Also, system jitter increases with the number of switches to be closed. PCSS technology combines very fast closure with subnanosecond delay, independence from circuit conditions, and very low jitter in switch closure. These characteristics allow synchronizing many switches with very low jitter.

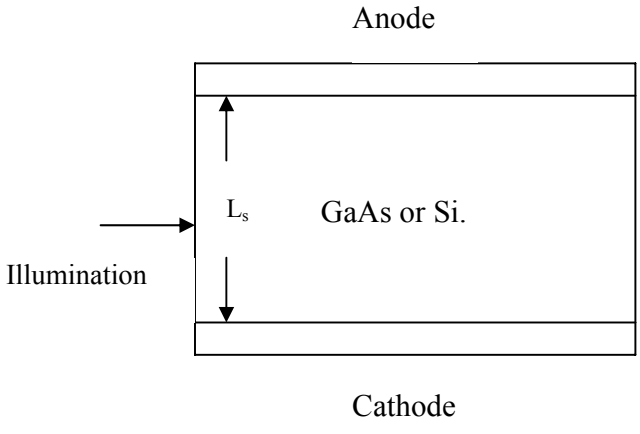

Fig. 2.8 A plain photoconductive switch.

PCSSs have been found to be useful in applications such as high voltage pulse generation and high power microwave generation [39-41]. In such cases gain and power are more important than speed of response, so the nonlinear avalanche-like lock-on effect [42-44], which occurs when semi-insulating (SI) GaAs is biased above approximately 5.0 kV/cm, is used to produce gains more than 100 times larger than that possible with operation in the linear mode [45,46]. The trade-off, of course, is that the device turn-off or recovery time is substantially longer in the nonlinear mode as compared to the linear mode [47,48]. Also, current filaments that occur during lock-on reduce the lifetime of the PCSS [49,50]. Thus, lock-on must be avoided in PCSS devices designed for use at GHz frequencies. Moreover, ways of increasing the breakdown strength of the PCSS are necessary for high power applications. Studies have shown that opposed contacts with 20 um thick n^+ layers can increase the breakdown field of a GaAs PCSS [40,51].

The physical properties of GaAs and Si are compared in Table 2.1. Compared with GaAs, Si has lower fabrication process costs and higher stability of the devices that are made from it; however, GaAs was selected for this project over Si for the following reasons. First, GaAs has a larger bandgap than Si (approximately 1.42 eV compared with 1.12 eV for Si). The larger bandgap of GaAs results in much lower leakage current and correspondingly higher dark resistivity. The dark resistivity of SI-GaAs is in the range of 10^7 to 10^8 Ω-cm [52]. Also, a larger bandgap also results in higher breakdown electric field for GaAs. Furthermore, the maximum current density of GaAs is higher than in Si, which reduces the chance of thermal run-away. Also, higher saturated drift velocity and electron mobility for GaAs lead to higher photoconductive switch speeds than with Si.

Finally, GaAs is a direct bandgap material, so that the optical processes are much faster than in the indirect bandgap material silicon.

Property	Units	Si	GaAs
Physical and Electronic			
Bandgap at 300K	eV	1.12	1.43
Thermal Conductivity	W/cm-K	1.5	0.5
Saturated Drift Velocity	cm/sec	$1.0*10^7$	$2.0*10^7$
Drift Mobility - Electrons	cm/V-sec	1500	8500
Drift Mobility - Holes	cm/V-sec	450	400
Max. Operating Surface Electric Field	KV/cm	90	150
Bulk Breakdown Electric Field	KV/cm	200	300
Maximum Current Density	KA/cm^2	50	500
Maximum Current Per Unit Width	KA/cm	0.5	500
Dielectric Constant	-	11.8	12.8
Max. Junction Temperature	$^{\circ}C$	~250	~300

Table 2.1 Property comparison of GaAs and Si.

In order to achieve our OE Class AB push-pull PA at 10 GHz frequency, a new design of PCSS, which does not experience the lock-on effect, is needed. Since we have a linear PA, the electrical output waveform must be able to follow the intensity of the optical pulse; therefore, fast turn-on time and turn-off time are needed. In Chapter 3, we will describe our new GaAs PCSS and OE Class AB push-pull PA.

Chapter 3 Theory of GaAs PCSS and OE Class AB Push-Pull PA

In this chapter, we will first discuss the characteristics and theory of our GaAs PCSS. Then, we will apply our new GaAs PCSS design to our OE Class AB push-pull PA, which we will discuss in the second section. In the third section, we will discuss stacking and multi-layer GaAs PCSSs in order to increase the overall system output power.

3.1 Theory of GaAs PCSS

A general description of GaAs PCSS devices will be given first in this section. Also, we will discuss the GaAs PCSS physics. Finally, we will describe our new design of GaAs PCSS, which is required to meet our specification for the OE Class AB Push-Pull PA at 10 GHz (X band) operation.

3.1.1 GaAs PCSS device description

GaAs, a III-V compound semiconductor, is very popular for use in discrete and integrated circuits for microwave, millimeter-wave, optoelectronic, and digital applications. The resistivity of GaAs can be altered by illuminating the surface of the material with an optical source whose photon energy is greater than the GaAs bandgap energy. The absorbed photons generate electron-hole pairs with quantum efficiency near

unity. This effect, called photoconductivity, has been used for numerous applications, principally in high speed photodetectors and high power switches.

Different choices of GaAs PCSS geometry have been studied for different purposes [38,51]. Fig. 3.1 shows different GaAs geometries, including lateral PCSS, planar PCSS, and opposed contact PCSS. The lateral PCSS, shown in Fig. 3.1(a), is the

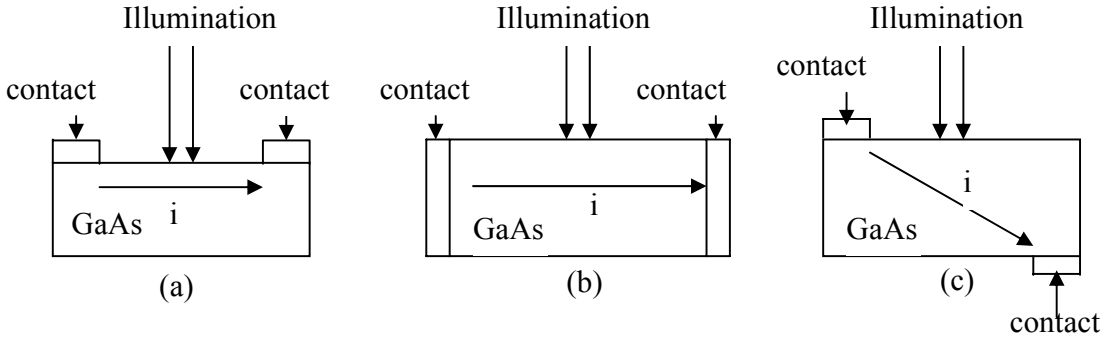

Fig. 3.1 Different configurations of GaAs PCSS, (a) lateral PCSS, (b) planar PCSS, and (c) opposed contact PCSS.

simplest structure for coupling the optical energy into the switch. For uniformly illuminated linear switching, the minimum resistance is reached almost immediately. However, a disadvantage of this geometry is the exposure of the wafer surface to the full electric field. For GaAs, the electric breakdown strength of a surface is usually significantly lower (by approximately one-half) than the bulk electric breakdown strength (Table 2.1). The planar PCSS, shown in Fig. 3.1(b), increases the breakdown voltage by reducing fields near the switch surface. Similar to the lateral PCSS, light can be absorbed in the active region and the lowest resistance can be achieved immediately. Finally, the opposed contact PCSS shown in Fig. 3.1(c) was developed to improve the breakdown voltage even further. With the same dimensions as for the planar and lateral PCSSs, the opposed contact PCSS has higher breakdown voltage because the distance between the

two contacts is longer. However, the opposed contact PCSS is not suitable for X-band microwave applications because the electrode distance needs to be short for high frequency response. If that is the case, some of the optical power applied to the top surface of the opposed contact PCSS may not be absorbed due to the shorter electrode distance. Therefore, a planar GaAs PCSS (Fig. 3.1(b)) was chosen for our 10 GHz (X-band) OE Class AB push-pull PA.

The two contacts of the PCSS can be either ohmic or Schottky contacts. To form ohmic contacts, n^+ layers need to be doped under the contacts; this forms electron injection contacts. Thus, the contact injection efficiency is close to one, which also improves the gain of the device. However, the trade-off of using ohmic contacts is that the sweep-out time increases, meaning a longer turn off time. With Schottky or rectifying contacts, since we do not have electron injection at the contacts, an increase in the input optical power is required in order to compensate for the lack of electron injection; therefore, we sacrifice gain in order to decrease the sweep out time (or reduce the turn-off time). For our purposes, Schottky contacts are needed for the speed of response required at 10 GHz.

In Fig. 3.1(b), Schottky contacts are placed on both sides of the semi-insulating (SI) or intrinsic GaAs bulk material, which physically forms two Schottky diodes, as shown in Fig. 3.2. Before illumination, the Schottky diode on the cathode end is forward biased and the Schottky diode on the anode end is reversed biased so the device does not conduct at small voltage. However, due to the small reverse breakdown strength of Schottky diodes, current could start to flow at low voltage. For our switch, however, current flow will be limited because of the high resistivity and breakdown voltage of the

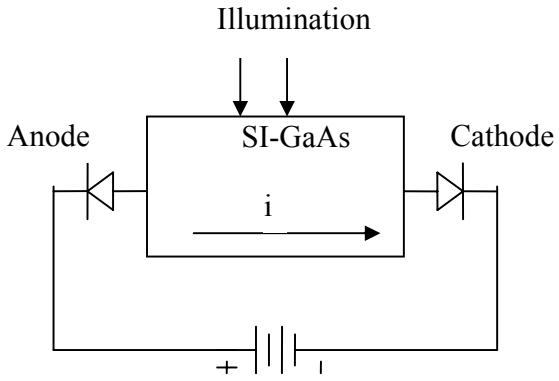

Fig. 3.2 Two Schottky diodes were formed when the bias voltage is applied to the switch based on Fig. 3.1 (b).

semi-insulating (SI) or intrinsic GaAs bulk material, even though both Schottky diodes can conduct. With illumination, large electron and hole concentrations decrease the resistivity of the GaAs bulk material, so current can then flow through the device, turning on the switch.

3.1.2 GaAs PCSS physics

Semi-insulating (SI) GaAs, just like intrinsic GaAs, has a high resistivity without illumination. This results in very little leakage current when the switch is off. Single crystals of semi-insulating or intrinsic GaAs have been grown by many techniques utilizing melt and solution approaches, including horizontal Bridgman (HB) and vertical Bridgman (VB), liquid-encapsulated Czochralski (LEC), liquid-encapsulated Kyropoulous (LEK) and magnetic LEC (MLEC). The Bridgman technique is dominant

in material quantity; however, the LEC-growth technique has become even more popular since 1990 [27].

Different defects are associated with different growth techniques; therefore, compensation mechanisms are usually required in order to produce the SI-GaAs material. For example, SI-GaAs grown by the LEC method has one defect, called a deep donor level EL2 trap. Experiments have shown that EL2 centers are electrically neutral when occupied by electrons and they are positively charged when they release these electrons [53,54]. Thus they behave like donors. For GaAs to exhibit semi-insulating behavior, a shallow acceptor impurity, usually carbon (C) is doped to compensate the deep donor EL2 defect. This is called the deep donor, shallow acceptor (DDSA) compensation process. Fig. 3.3 shows the energy level diagram for this compensation mechanism.

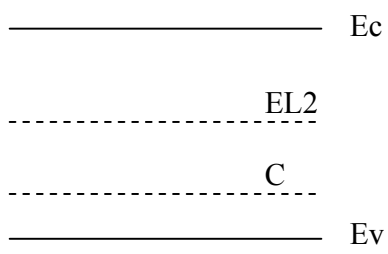

Fig. 3.3 Energy level diagram for the DDSA compensation mechanism.

For the PCSS shown in Fig. 3.1(b) based on SI-GaAs material with the DDSA compensation mechanism or intrinsic GaAs, the electron is used as the majority carrier because of its higher drift velocity and mobility compared with those of the hole. According to the electric field dependence of electron drift velocity in GaAs, shown in Fig. 3.4 [39], at low electric fields, generally smaller than 5 KV/cm, the electron drift velocity is linear with the electric field, and it reaches its maximum, around $1.5*10^7$

cm/sec, when the electric field is approximately 5 KV/cm. At higher electric fields, the electron drift velocity decreases until the electric field is around 15 KV/cm, at which the

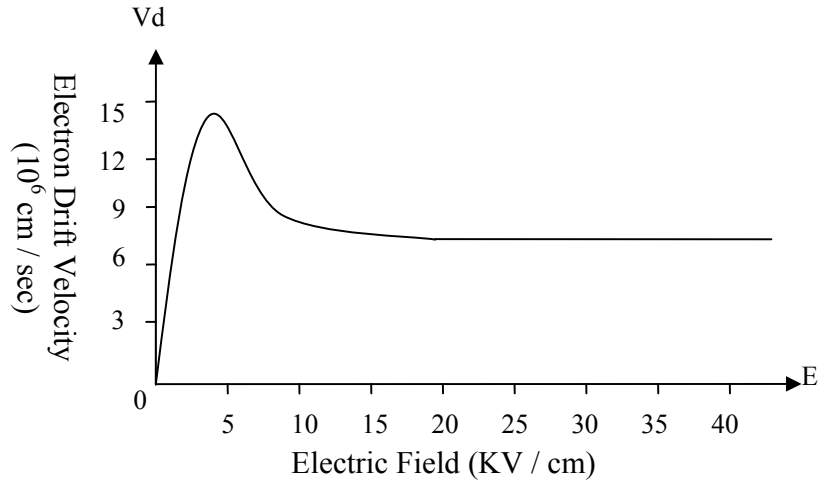

Fig. 3.4 Electric field dependence of electron drift velocity in GaAs.

electron drift velocity reaches its saturated value around $7.7*10^6$cm/sec. This happens because of the nature of the energy band structure of GaAs.

Fig. 3.5 shows the energy band E-K diagram of GaAs. There are two valleys in GaAs's energy band, the upper valley and the lower valley. The energy difference between them is around 0.31 eV. Electrons in the lower valley generally have higher mobility than in the upper valley because they have lower effective mass in the lower valley than in the higher valley. Under the influence of a small electric field, most of the electrons stay in the lower valley shown in Fig. 3.5(a) and the electron drift velocity υ_e increases linearly with electric field. Thus, the electron mobility μ_e is equal to

$$\mu_e = \frac{\upsilon_e}{E}. \qquad (3.1)$$

As the electric field grows, those electrons in the lower valley obtain enough energy to move into the upper valley shown in Fig. 3.5(b), where they have lower mobility. That is why we see the velocity drop as the electric field becomes greater than 5 KV/cm. If the electric field is increased further, most of the electrons will be in the upper valley as shown in Fig. 3.5(c) and we will see almost constant drift velocity, as shown in Fig. 3.4.

The region where the electron drift velocity decreases with an increase in electric field is called the region of negative differential mobility. In this region, the mobility is equal to the derivative of the electron drift velocity with respect to the electric field

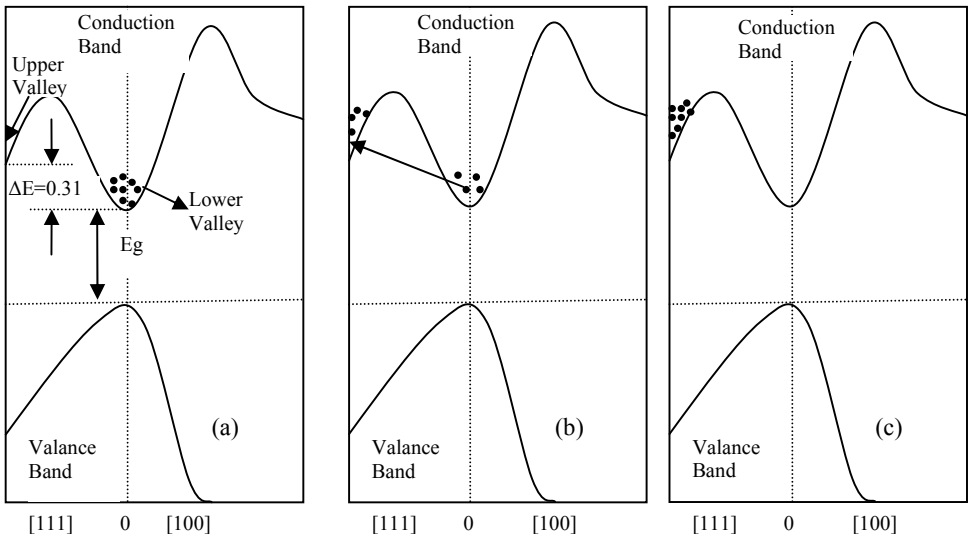

Fig. 3.5 The energy band E-K diagram of GaAs shows the electron distribution in different electric field; (a) E < 5KV / cm; (b) 5 KV / cm < E < 15 KV /cm; (c) E > 15 KV / cm.

$$\mu_e = \frac{\partial \upsilon_e}{\partial E} \qquad (3.2)$$

If the electric field is above 15 KV/cm, the electron drift velocities are constant at the thermally limited saturation value $\upsilon_{e\,sat}$, usually around $7.7*10^6$ cm/sec. Thus, Equation (3.1) becomes

$$\mu_e = \frac{\upsilon_{esat}}{E} \qquad (3.3)$$

and the carrier mobility varies inversely with the electric field. With higher electric field, lower electron mobility can be expected.

As the bias voltage across the SI-GaAs PCSS shown in Fig. 3.1(b) is increased from zero, the device goes through two modes of operation, beginning with the linear mode. The linear mode is characterized by one electron hole pair produced by each photon absorbed. Thus, the conductivity of the SI-GaAs PCSS is linearly proportional to the total photon flux entering the device and the PCSS conductivity approximately follows the variation of intensity of the optical pulse. The switch closes as the optical intensity increases and the conductivity of the switch increases. The closure time of the switch is determined by the rise time of the laser pulse. The switch turns off or opens when the optical pulse is removed. The turn off time is determined by electron and hole lifetimes, which are determined by various material and device parameters.

When the bias electric field across the switch exceeds approximately 4-8 KV/cm [38], the transition occurs to a nonlinear mode that exhibits high gain and long conduction times. This nonlinear mode is called controlled breakdown or lock-on. In this mode, instead of following the light intensity pulse shape, the switch turns on and stays on (lock-on) until the lock-on mechanism terminates. Some type of gain mechanism occurs because there are many more carriers generated than can be created

directly by the incident photons. Furthermore, the switch continues to conduct for many recombination times after the optical trigger has been removed. At present, lock-on operation has only been found in GaAs and InP, which are both direct bandgap semiconductors with a satellite valley in the conduction band that leads to negative differential resistance (NDR). For bulk NDR, negative resistivity is associated with microscopic bulk semiconductor properties, such as field-enhanced trapping, impact ionization of shallow impurity levels in compensated semiconductors, and electron transfer from a lower valley to higher valleys in the conduction band. A semiconductor exhibiting bulk NDR is inherently unstable, because a random fluctuation of carrier density at any point in the semiconductor produces a momentary space charge that grows exponentially in time.

The physics of the lock-on effect is not well understood. One explanation of this phenomenon is the so called field dependent trapping/de-trap phenomenon in SI-GaAs. Using Fig. 3.3, consider the trap-to-band generation and recombination. At low field, optical illumination excites the electrons in the EL2 trap to obtain enough energy to jump to the conduction band; thus, the device turns on. When the optical pulse is removed, electrons in the conduction band would stay for a period of time, called electron lifetime, and then recombine with the trap. The electron life time, τ_e, can be determined by [55]

$$\tau_e = \frac{1}{N_t * \upsilon_e * \delta} \qquad (3.4)$$

where N_t is the trap concentration, υ_e is the average thermal velocity for electron, and δ is the trap capture cross section area.

At high fields, approximately from 4-8 KV/cm, the trap capture cross section area, δ, becomes larger than that at low field (field enhanced trapping). Therefore, the electron lifetime time, τ_e, would decrease according to Equation (3.4) at high fields, which results in shorter recombination time. Decreasing the recombination time also indicates that the photo-generated electrons can get trapped easier at high fields compared with that at low fields. The temporary increase of the device resistance due to the trap phenomenon results in the temporary decrease of current. Instead of returning to the original carrier concentration equilibrium (before illumination), the device would settle down with a new steady state carrier concentration equilibrium because of the electron de-trap phenomenon, due to impact ionization and trap-band tunneling. Therefore, lock-on occurs.

Collective impact ionization and current controlled negative differential resistance (CCNDR) have been studied to explain the current filaments observed in nonlinear SI-GaAs PCSSs [56-58]. NDR devices can be classified into two groups: voltage controlled NDR and current controlled NDR. Voltage controlled NDR devices include the tunnel diode and transferred electron devices. Current controlled NDR can be found in thyristor devices. Because of NDR, the semiconductor, initially homogeneous, becomes electrically heterogeneous in an attempt to reach stability. Next, we will show that for a SI-GaAs PCSS exhibiting CCNDR, high gain and high current filaments will form and longer turn off time can be expected.

For CCNDR, the initial positive differential resistivity decreases with increasing field; that is, $d\rho/dE < 0$, as shown in Fig. 3.6(a). If a region of the device has a slightly higher field, as shown in Fig 3.6(a), the resistance there is smaller. Thus, more current

will flow into it. This results in an elongation of the region along the current path, and finally in the formation of a high current filament running along the field direction, as shown in Fig. 3.7(b). The current filament usually is due to the carrier-carrier scattering effect leading to collective impact ionization. Therefore, the avalanche-like lock-on phenomenon leading to a high gain mechanism will be observed in nonlinear SI-GaAs PCSS. Then, it will take substantially longer recovery time for the switch to return to its normal state.

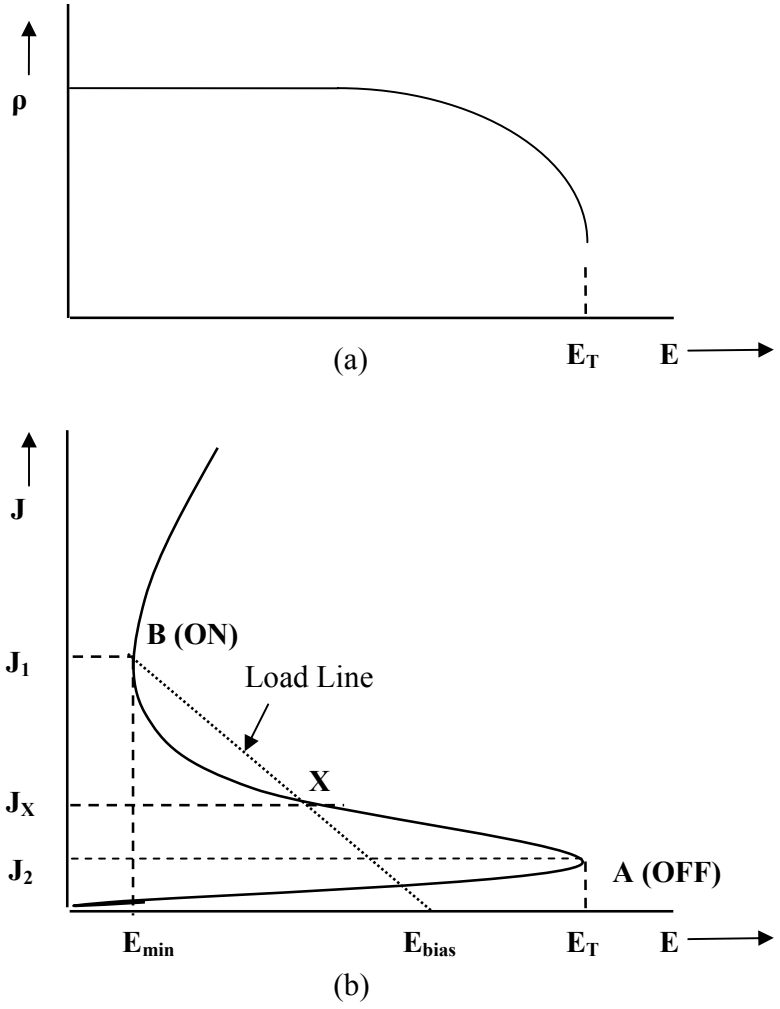

Fig. 3.6 (a) Negative differential resistivity (NDR), dρ/dE < 0, (b) A typical J-E plot for CCNDR with S-like curve and load line.

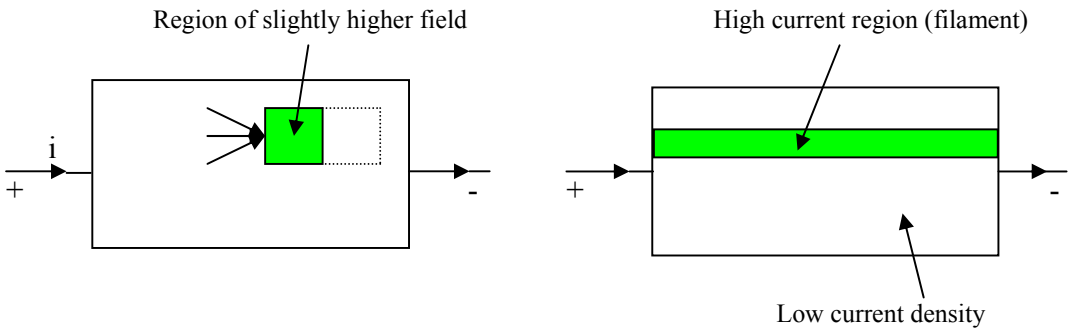

Fig. 3.7 Formation of high current filament in a CCNDR; (a) a region with slightly higher field, (b) a high current filament running along the field direction.

Fig. 3.6(b) shows a typical instantaneous J-E plot and load line for a device with CCNDR. This plot can also be used to explain the nonlinear operation of the SI-GaAs PCSS. If the bias electric field, E_{bias}, is between the breakdown electric field, E_T, and the minimum lock on field, E_{min}, the dark current density (before illumination) is smaller than J_2 (see region A) and the device is in the OFF state. After the illumination is applied, the optical trigger drives the system from the OFF state through the unstable state, J_x (or region X), to the high current density state, J_1 (region B), which is the ON state of the switch. After the light trigger is removed, the device will stay ON because of the avalanche process, and the electric field across the device will be at E_{min}, often called the lock-on field. This situation will remain until the electrical signal across the switch is removed.

3.1.3 Design features of SI-GaAs PCSS for X-band operation

As mentioned above, the nonlinear avalanche-like lock-on effect, which can occur when semi-insulating (SI) GaAs is biased above approximately 5.0 kV/cm, is used to produce gain more than 100 times larger than that possible with operation in the linear mode. The trade-off is that the device turn-off or recovery time is substantially longer in the nonlinear mode than in the linear mode. Thus, lock-on must be avoided in PCSS devices designed for use at GHz frequencies. There are two ways to eliminate lock-on. The first is to use intrinsic GaAs instead of SI GaAs; however, the trade off is that the intrinsic GaAs is relatively harder to fabricate and more expensive than SI GaAs. The other way is to use sweep-out mechanism instead of recombination to remove photo-induced carriers if the lock-on phenomenon we discussed in the previous section is accurate.

There are two ways to remove photo-generated carriers. The first way is to use the natural recombination process of the material. For the switch and circuit to follow a very fast falling optical signal, the switch recombination time must be less than or equal to the falling optical signal. For our application, a 10 GHz optical pulse is a $1*10^{-10}$ second time pulse, which is faster than the electron and hole lifetimes of the SI-GaAs, which are $5*10^{-10}$ sec. and $6*10^{-9}$ sec., respectively. Therefore, natural recombination is not suitable for our problem. The second way is to use carrier movement to the electrodes in the applied electric field of the conducting switch. The carriers move at drift velocity and are removed at one electrode in a characteristic transit time. If the carriers are not re-injected at the opposite Schottky contact as they are swept out of the conducting region, they can be removed much faster than by natural recombination, depending on the geometry of the switch. The sweep-out mechanism instead of natural

recombination can ideally prevent the lock-on phenomena as we discussed last section, and also enable switch operation at X-band frequency.

The geometry of the designed PCSS is shown in Fig. 3.8. The material is LEC-grown DDSA GaAs containing equal concentrations (3.0 x 10^{15}/cm^3) of deep lying EL2 traps and shallow carbon acceptors to simulate SI-GaAs. The electrodes are copper with

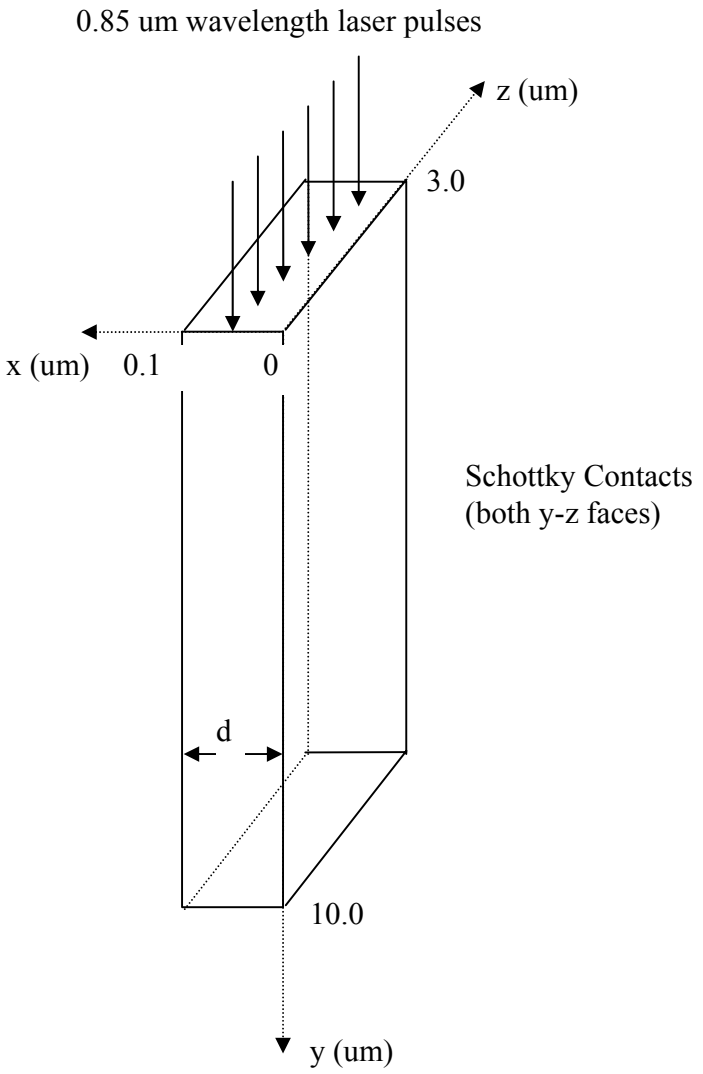

Fig. 3.8 The SI-GaAs photoconductive semiconductor switch (PCSS) in question. The upper face is uniformly illuminated by 0.85 um wavelength laser pulses.

work function 4.7 eV to simulate rectifying Schottky contacts with extremely small dark currents. The device is 10.0 μm tall, 3.0 μm deep, and only 0.1 μm wide in the direction of photocurrent flow. The 10.0 μm device height was chosen to ensure band-to-band absorption of at least 99% of the incident 0.85 μm wavelength light, whose absorption coefficient in GaAs is approximately 5.0 x 10^3 cm^{-1}. This is found by using the equation

$$\phi(y) = \phi_0 * e^{-\alpha y} \qquad (3.5)$$

where ϕ_0 is the total photon flux (photon/cm^2*sec) that enters the switch at y = 0, $\phi(y)$ is the total photon flux in the switch at depth y, and α is the absorption coefficient of GaAs.

The 3.0 μm depth was chosen to provide a large enough cross-sectional area to ensure that the photocurrent density would not exceed the 500 kA/cm^2 allowable maximum for GaAs, beyond which thermal runaway could occur.

Finally, the narrow 0.1 μm device width d (between the electrodes) was necessary to ensure the fast removal of photocarriers by sweep-out in the electric field associated with the applied voltage. This feature is necessary to minimize the probability of collective impact ionization and subsequent lock-on during illumination, which would render the device too slow for microwave applications. From ballistic transport theory [27], when an electron encounters a sufficiently high electric field in a very narrow region, it may not undergo the collisions needed to produce the steady-state speeds shown in Fig. 3.4. Instead, higher velocities may be reached, resulting in shorter transit times. At room temperature, the mean free path (m.f.p.) between collisions of an average electron in GaAs is approximately 0.1 um. For this reason, 0.1 um was chosen as our electrode separation distance.

3.2 Opto-electronic (OE) Class AB push-pull power amplifier

In this section, we will first describe the basic Class B and AB push-pull PAs. Then, a hybrid experimental circuit that uses photodiodes and SiGe heterojunction bipolar transistors (HBTs) developed by our group [59] will be described. The operation frequency for this test platform ranged up to 4 GHz. Finally, the design of a fully OE Class AB push-pull PA for 10 GHz operation will be described.

3.2.1 Basic circuit description of Class B and AB push-pull PAs

The purpose of the microwave PA is to amplify a high frequency sinusoid. Thus the output voltage must also be a sinusoid, i.e., a signal having both positive and negative values. One power amplification stage that can do this is called the "complementary-pair" or "push-pull", emitter follower configuration, also known as Class B PA, as shown in Fig. 3.9. The active devices, Q_1, and Q_2, can be BJTs, MOSFETS, or HEMTS. When the input signal is positive, the lower device, Q_2, remains cut off, and the upper device, Q_1, is driven into the active region by the input signal. The large signal output for positive input v_{in} becomes that of a simple follower, that is,

$$v_{out} = v_{in} - V_f$$

Similarly, when the input is negative, the upper device, Q_1, remains in cutoff, but the lower device, Q_2, is driven into the active region by the input signal. The output voltage under such condition becomes,

$$v_{out} = v_{in} + V_f$$

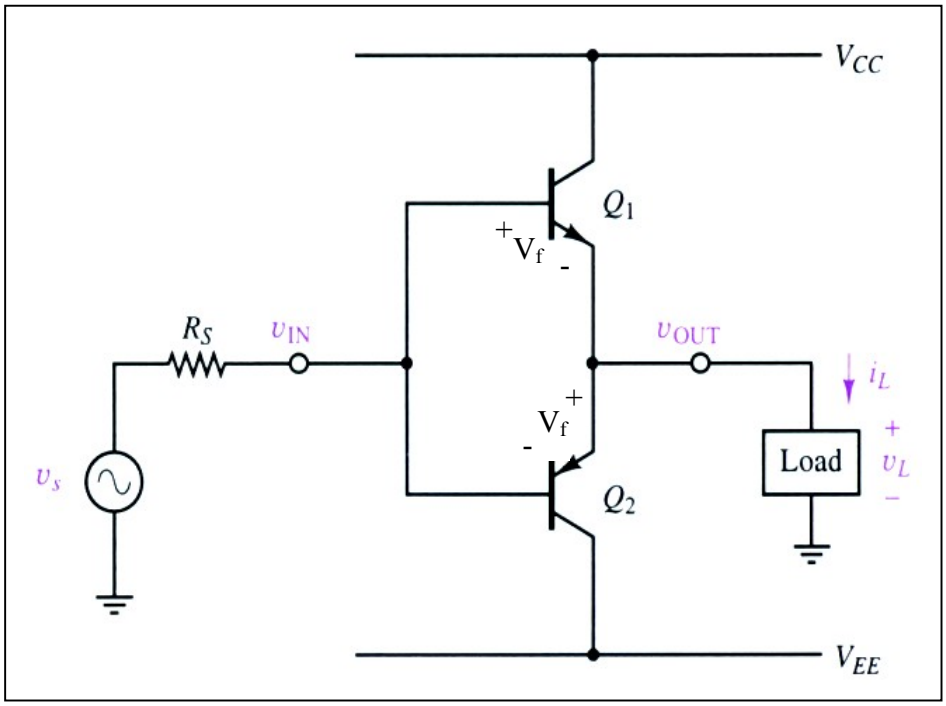

Fig. 3.9 A complementary pair or push-pull Class B PA.

Note that v_{out} is equal to zero if the magnitude of v_{in} is less than the base-emitter turn-on voltage V_f.

Fig. 3.10 shows the complete transfer characteristic of the output stage, including both positive and negative input voltages. Near the origin, where $|v_{in}| < V_f$, the slope of the transfer characteristic changes abruptly to nearly zero. This is called the crossover distortion region. The crossover distortion illustrates the nonlinear behavior of the amplifier and results in an output signal that is not an exact replica of the input signal.

The problem of crossover distortion in a Class B amplifier can be solved by biasing the complementary-pair devices into the active region, just above cutoff. This can be done with two diodes, as shown in Fig. 3.11. The diodes are kept forward biased

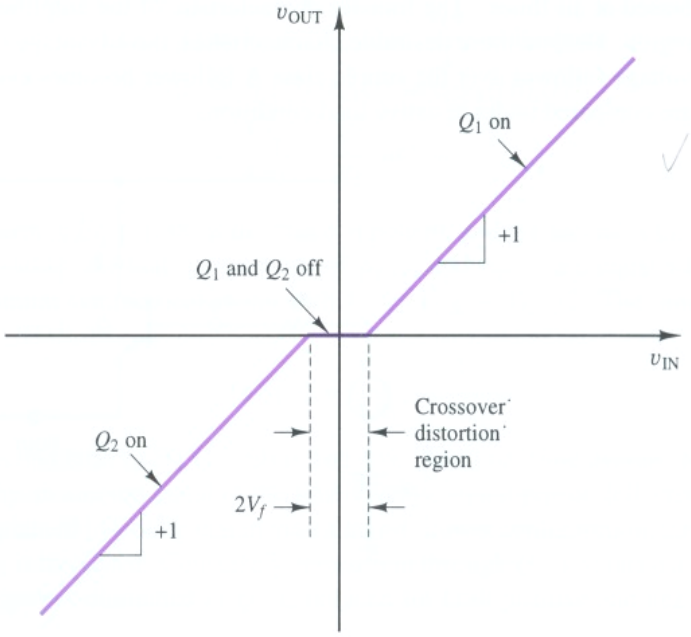

Fig. 3.10 Transfer characteristic of the Class B push-pull PA.

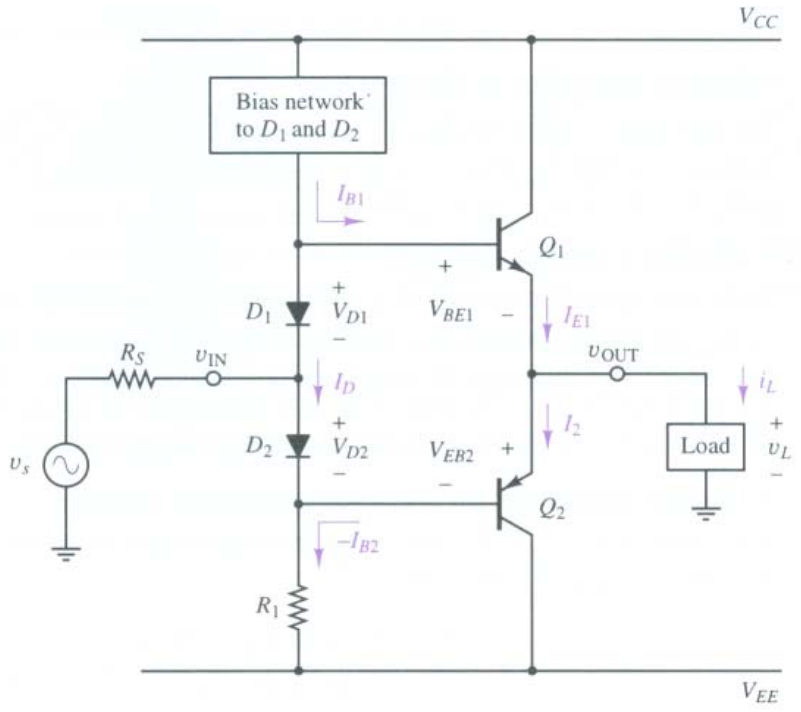

Fig. 3.11 Circuit with two diodes added forming a Class AB PA.

by the bias network and the resistor R_1. The series combination of D_1 and D_2 is connected in parallel with the base-emitter junctions of Q_1 and Q_2 so that

$$V_{BE1} + V_{BE2} = V_{D1} + V_{D2} = 2V_f$$

where V_f is the turn-on voltage of the diodes.

D_1 and D_2 will behave as constant voltage sources of value V_f when an input signal is applied. When v_{in} is positive, Q_1 will be driven into its active region, with v_{out} given by

$$v_{out} = v_{in} + V_{D1} - V_{BE1}$$

$$= v_{in} + V_f - V_f = v_{in} \qquad (3.6)$$

When v_{in} is negative, Q_2 will be driven into its active region with v_{out} given by

$$v_{out} = v_{in} - V_{D2} + V_{BE2}$$

$$= v_{in} - V_f + V_f = v_{in} \qquad (3.7)$$

Thus, the problem of crossover distortion is eliminated by the use of the two biasing diodes.

The price paid for reducing the crossover distortion is a small decrease in amplifier power efficiency, due to the additional power loss in the diodes. This circuit is often called the Class AB PA.

3.2.2 OE Class AB microwave amplifier test platform [59]

As mentioned in Chapter 2, the use of p-type and n-type transistor pairs is needed to fashion a traditional Class AB push-pull PA because the polarity of the input electrical

signal is both positive and negative. However, the n-type transistor transconductance is an order of magnitude greater than that of the p-type transistor due to the difference in electron and hole mobilities, which limits the operating gain and efficiency of the push-pull pair. One way to solve this problem is to use only n-type transistors. To demonstrate the concept, we assembled a hybrid system consisting of photodiodes and NPN SiGe heterojunction bipolar transistors (HBTs). The photodiodes were used because optically gated SiGe HBTs are not currently available.

The hybrid table-top system consists of optical and electrical sections. Fig. 3.12 illustrates the optical portion of the system. The purpose of this section is to convert an input optical signal to an electrical signal to drive the HBTs. The optical communication standard OC-192 was used to design this section. The DFB laser diode shown in Fig.

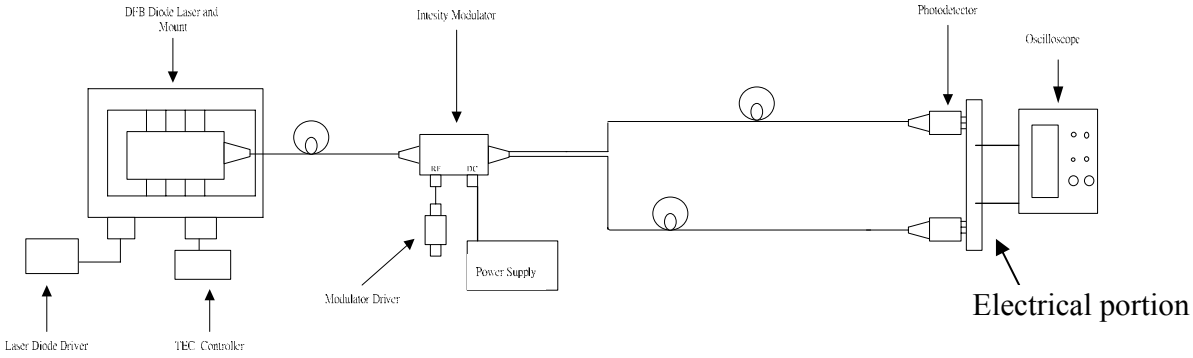

Figure 3.12 Schematic of the optical portion of the test platform.

3.12 was used to produce the optical power, which was modulated using the dual output laser intensity modulator ($LiNbO_3$ External Modulator). This produces two light beam pulses at the output of the modulator that are 180˚ out of phase. The two pin photodiodes were utilized to convert the optical power to electrical power. All of the optical connections were linked by optical fibers.

Fig. 3.13 shows the electrical portion of the system, which is the Class AB push-pull PA. The ideal inputs to the circuit are two electrical pulse trains coming from the photodiodes in the optical portion of the system. These two electrical waveforms are ideally positive and 180˚ out of phase. Therefore, two n-type SiGe HBTs could be used, thereby eliminating the transconductance difference between n-type and p-type transistors. SiGe HBTs were used for several reasons [59]. The first reason is because of its high frequency operation capability. Second, they are compatible with silicon technology, allowing the integration of logic functions. Third, the thermal conductivity of SiGe is approximately three times higher than that of GaAs. Thus, thermal design of the system is simpler. Finally, the cost of silicon-based devices is much lower than that of GaAs FET devices.

The bias networks shown in Fig. 3.13 were needed in order to accurately drive the two SiGe HBTs into the active region. We used $-V_{cc}$ for the emitter DC power of HBT2

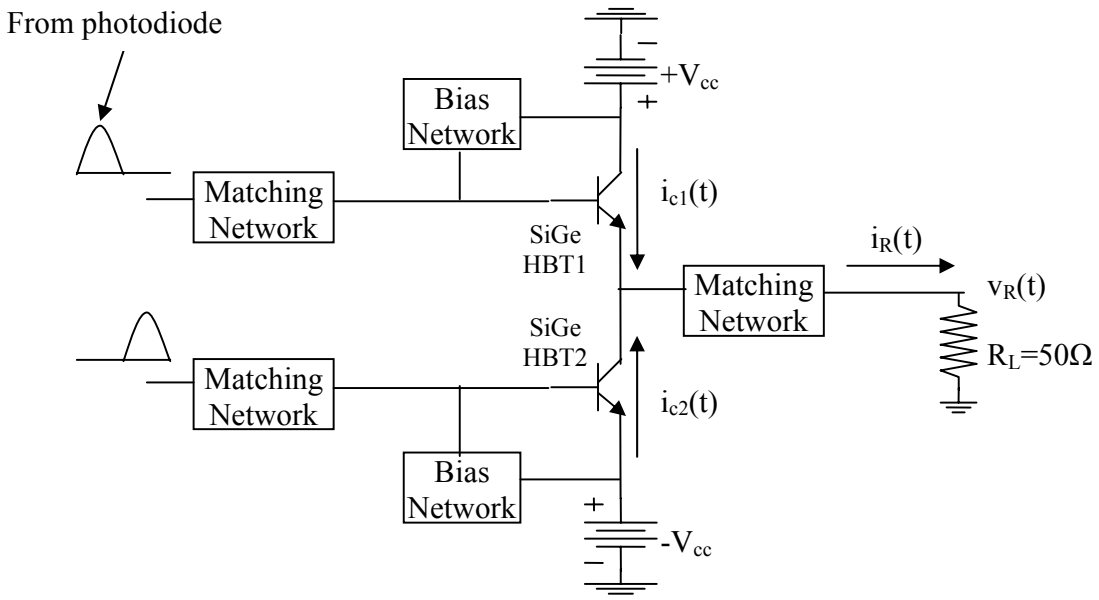

Fig. 3.13 Schematic of the electrical portion (Class AB push-pull PA) of the test platform.

in order to produce the negative portion of the sinusoidal waveform for the load voltage. This circuit was built without input and output matching networks in order to study the circuit over a range of frequencies. However, an amplifier built without input and output matching networks will have reflection losses consuming 1/2 to 2/3 of the input power. Thus, we expected the measured efficiencies to be much lower than the theoretical values.

A computer simulation study of the table-top system showed that up to 53 % power added efficiency (PAE) can be achieved at 2 GHz, which is better performance than the traditional Class AB PA. However, since matching networks were not included in the experiment, the measured efficiency was only 14.1 % at 2 GHz, 8.5 % at 3 GHz, and 2.9 % at 4 GHz. To improve the circuit operation, the laser diode needs to be integrated with the laser intensity modulator and an integrated optical waveguide needs to be used to connect the components, thus implementing it as a monolithic microwave integrated circuit (MMIC). Also, matching networks need to be included in the MMIC to reduce the reflection losses. Another way to improve the circuit is to utilize suitable photoconductive semiconductor switches instead of the photodiodes and SiGe HBTS, as discussed in the following section.

3.2.3 OE Class AB push-pull PA with our newly designed GaAs PCSSs

As explained in the previous section, an OE Class AB push-pull PA table-top test platform was studied by our group. Photodiodes and SiGe HBTs were used at frequencies up to 4 GHz. As Fig. 3.13 shows, the test platform was formed with HBT1 in the common-emitter mode in the upper branch and with HBT2 in the common-

collector or emitter follower mode in the lower branch. In this system arrangement, the upper and lower branches are not symmetrical, which reduces the gain mechanism, causing lower circuit efficiency. Thus, high efficiency operation at 10 GHz was not possible for the table-top test platform. To improve matters, the photodiodes and HBTs were replaced with photoconductive semiconductor switches (PCSS), as shown in Fig. 2.4 and repeated in Fig. 3.14 fro convenience. As mentioned in section 3.1.3, a properly

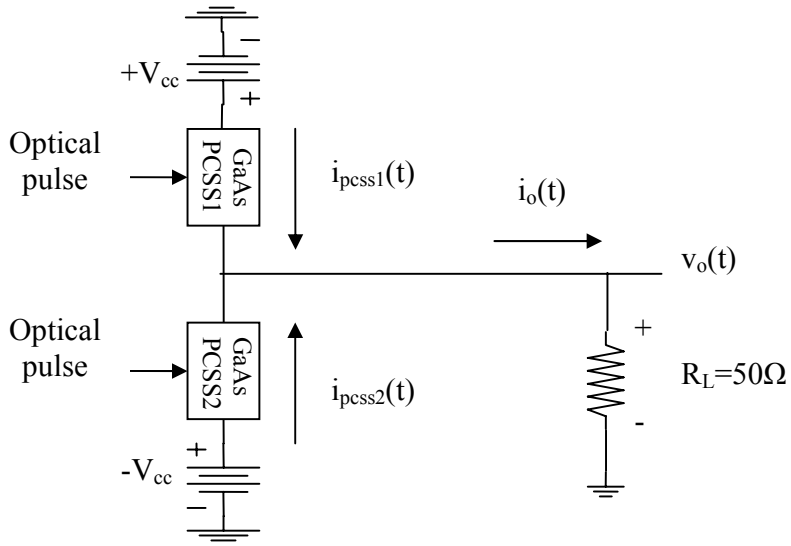

Fig. 3.14 New schematic of an OE Class AB push-pull Microwave PA with PCSSs.

designed PCSS should be able to operate at 10 GHz. Also, the input matching network and current controlled gate drive circuits needed for SiGe HBTs are eliminated since there is no electrical signal before the PA, which reduces the complexity of the system.

The optical signals driving the photoswitches PCSS1 and PCSS2 are assumed to be ultrafast laser pulses, which can be produced either by modulating the laser internally, so that the laser produces the pulses directly, or by externally modulating the output intensity of a continuous wave (CW) laser with a dual output Mach-Zehnder beam

modulator, as was done in the hybrid system. In either case, the photoswitches are assumed to be illuminated by a pair of laser optical pulse trains that are 180 degrees out of phase with each other. Thus, to produce a 10.0 GHz output electrical signal $v_o(t)$, each optical pulse train would consist of 50.0 ps-wide pulses with a 100.0 ps period. Fig. 3.15 shows the resulting photocurrents and output voltage. With the lower branch of Fig. 3.14 biased with negative V_{cc} as shown, the negative half-sinusoid of the output voltage is generated. The output voltage and current can be written as

$$v_R(t) = V_R * \sin(wt)$$

$$i_R(t) = (V_R / R_L) * \sin(wt) .$$

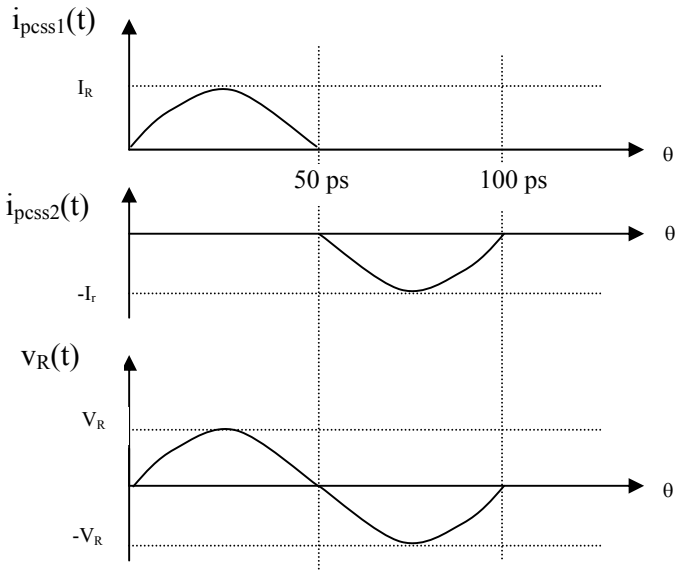

Fig. 3.15 Waveforms of an OE Class AB push-pull Microwave PA with PCSS.

Therefore, the average output power P_L can be found as

$$P_L = < i_R(t) * v_R(t) >$$

$$= < V_R * \sin(wt) * (V_R / R_L) * \sin(wt) >$$

$$= < (V_R{}^2 / R_L) * \sin^2(wt) > .$$

The time average of $\sin^2(wt)$ is 0.5, so the average output power can be written as

$$P_L = V_R{}^2 / 2R_L . \qquad (3.8)$$

To calculate the average input power, the DC supply in the upper branch supplies

$$P_{s+} = 1/T \int_0^{T/2} V_{cc} * i_{pcss1}(t) dt$$

$$= 1/T \int_0^{T/2} V_{cc} * V_R / R_L * \sin(wt) dt .$$

Since $\int_0^{T/2} \sin(wt) dt = 2/w = T/\pi$, we have

$$P_{s+} = (V_{cc} / \pi) * (V_R / R_L) .$$

The lower branch supplies the same average power. Therefore,

$$P_s = (2V_{cc} / \pi) * (V_R / R_L) \qquad (3.9)$$

and the efficiency of our circuit is

$$\eta = P_L / P_s$$

$$= (V_R * \pi) / (4V_{cc}) . \qquad (3.10)$$

The maximum efficiency will occur when the resistance of the PCSS is zero (ideal case), in which case $V_R = V_{cc}$ and equation (3.10) yields 78.5 % as the maximum efficiency for the circuit. This is the same value as for the electrical Class AB PA.

With our new design of OE Class AB push-pull PA, higher practical circuit efficiency at 10 GHz compared with the electrical Class AB circuits is expected because

the polarity and the transconductance problems are solved. Obviously, improving the practical efficiency by a factor of 2 will reduce the power requirements and the thermal management requirements by a factor of 2, which translate directly to the weight and volume of the system. Also, the OE PA solves the isolation problem. Furthermore, omitting the input matching network and gate drive circuits also increases the simplicity of the circuit.

3.3 OE Class AB push-pull power amplifier using stacking and multi-layer GaAs PCSSs

To produce greater output power levels, the input optical isolation should enable several PCSSs to be stacked, as in Fig. 3.16, to allow use of a higher source voltage, V_{cc}, which should lead to increased output power. Furthermore, since the ultimate goal of the project is to produce a compact, fully integrated MMIC, the multi-layer GaAs photoconductive switch shown in Fig. 3.17 is proposed. Using this structure instead of stacking several PCSSs, higher breakdown voltages should also be achieved, which is necessary to increase the output power of our new OE PA. Fig. 3.17 shows a three-layer device in which each active layer would be 0.1 um thick as in the discrete PCSS; thus, the device should operate well at 10 GHz frequency.

One expected problem with the stacked PCSS approach illustrated in Figs. 3.16 and 3.17 is that when we illuminate the multi-layer PCSS or stacked PCSS with the same amount of peak optical intensity that was used in the single PCSS structure, the total on-state voltage drop across the multi-layer PCSS or stacked PCSSs will be higher than that

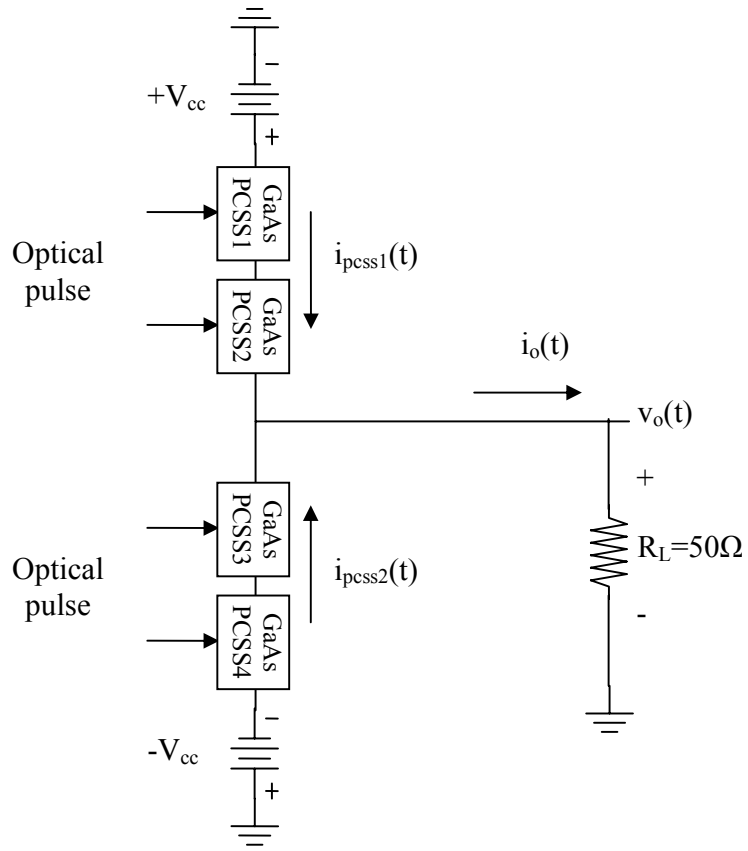

Fig. 3.16 OE Class AB push-pull microwave PA with stacked PCSSs.

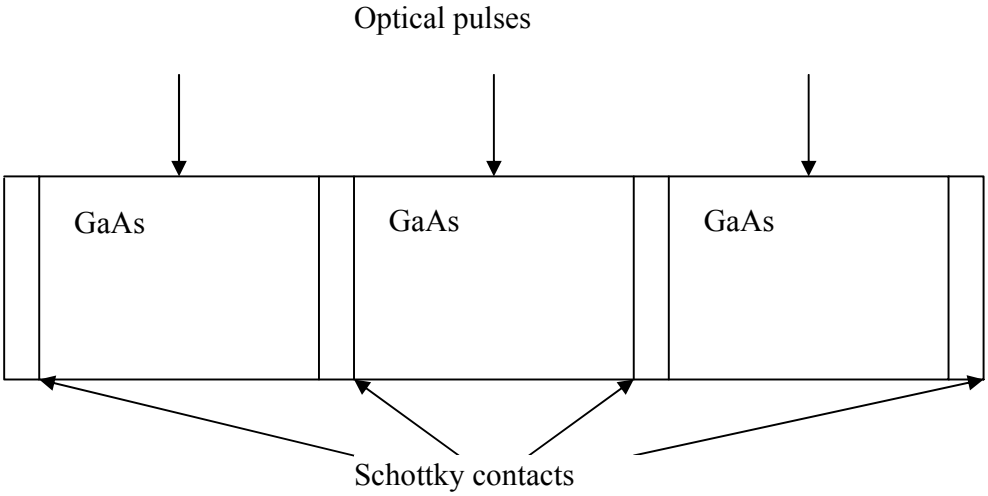

Fig. 3.17 Three layer GaAs PCSS structure.

of a single PCSS structure. The reason for this is that each PCSS has an on-state resistance when illuminated; these on-state resistances will be in series, which will cause the total on-state resistance to increase. Higher on-state resistance results in higher on-state voltage drop across the PCSSs, which decreases the circuit efficiency.

There are two ways to solve this problem. The first method is to increase the optical peak intensity in order to lower the on-state resistance of the multi-layer PCSS structure. However, increasing the optical peak intensity will also increase the current density in our PCSS which would increase the chance of the device thermal runaway. Therefore, in order to reduce the device resistance and also maintain the maximum allowable current density in the device, we suggest the second method, which is to increase the device depth, z, shown in Fig. 3.8, while the individual layer or device width, d, remains the same. According to the resistance versus resistivity relationship for a semiconductor [60], as shown in equation (3.11), if we increase the effective electrode width by using the multi-layer PCSS, we have to increase equally the same amount of the current flowing area, A, in order to keeping the resistance constant. Increasing the device depth, z, would accomplish that. This also maintains constant current density in the PCSS, which avoids the thermal runaway problem.

$$R = \frac{\rho * d}{A} \qquad (3.11)$$

For example, Fig. 3.18 shows a two-layer GaAs PCSS structure with three Schottly contacts located at x = 0, 0.1, and 0.2 um. In this case, the total device width d' = 2d, ie 0.2 um. In order to maintain the same device resistance and current density

while using equal amounts of laser peak intensity, the device depth, z, needs to be increased to 6 um instead of 3 um, as in a one layer PCSS device.

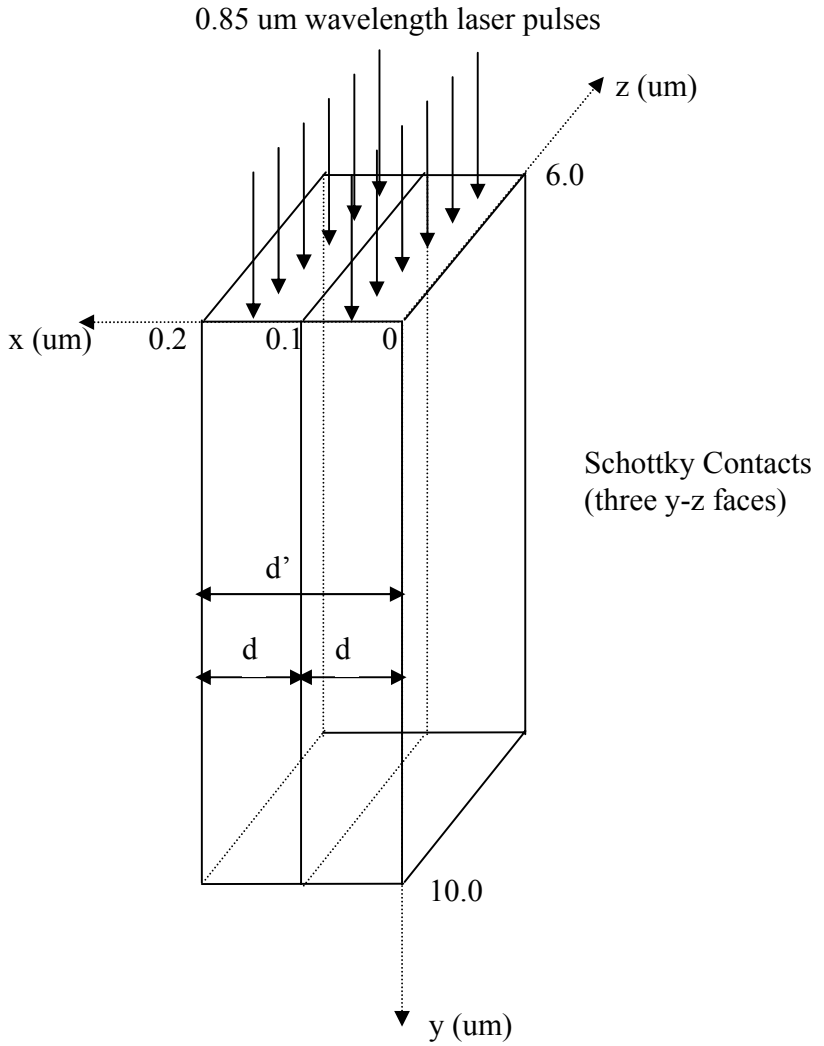

Fig. 3.18 Two-layer GaAs photoconductive semiconductor switch (PCSS). The upper face is uniformly illuminated by 0.85 um wavelength laser pulses.

Chapter 4 Simulation Results

In this chapter, simulation results obtained with the Atlas and Mixedmode software packages available from Silvaco Inc [61] will be presented. Atlas is a physics-based two-dimensional device simulator. It predicts the electrical behavior of user-specified semiconductor structures, and it provides insight into the internal physical mechanisms associated with device operation. Mixedmode is a circuit simulator that can be used to simulate circuits that contain semiconductor devices for which accurate compact models are unavailable, such as a device designed with Atlas.

The chapter is divided into five sections. In Section one, we discuss our intrinsic GaAs PCSS design and the simulation result for the dark I-V characteristic, obtained with Atlas software. In Section two, the photoconductive performance of the device, obtained with Mixedmode software, will be described. In Section three, the results from Section two will be discussed and analyzed. In Section four, the simulated performance of our OE Class AB push-pull PA design, obtained using Mixedmode software, will be presented. Finally, in Section five, the simulated performance of our OE Class AB push-pull PA design with multi-layer PCSS structures will be presented.

4.1 Physical modeling features and dark I-V characteristic

In order to avoid the lock-on effect, two methods were discussed in Section 3.1.3. However, since the Silvaco program does not support the lock-on effect (the physics of lock-on is still unclear), we are unable to determine if our novel SI-GaAs PCSS design

can successfully eliminate the lock-on effect with the Silvaco software (see Chapter 5 for the future extension). Therefore, for device and circuit studies with Silvaco software, our PCSS, shown in Fig. 3.8, was assumed to be fabricated from liquid-encapsulated Czochralski (LEC)-grown intrinsic GaAs instead of LEC-grown DDSA SI-GaAs containing equal concentrations ($3.0 \times 10^{15}/cm^3$) of deep lying EL2 traps and shallow (carbon) acceptors. The electrodes are copper (work function 4.7 eV) to simulate Schottky contacts with extremely small dark currents. The electron and hole lifetimes were set to $5*10^{-10}$ sec and $6*10^{-9}$ sec, respectively [38].

In order to correctly simulate the device, proper models for carrier transport, recombination, and avalanche must be included [62]. The carrier-carrier scattering effect on mobility is needed when the carrier concentration is high. For modeling the velocity saturation effect, parallel electric field dependent mobility must be included. Surface dependent mobility and concentration dependent mobility were also included. Recombination models are also important. The optical model in Atlas is utilized to include band-to-band recombination. Auger recombination is also included because of the potentially high current density in our device. Finally, the Schockley-Read-Hall model is included to account for the trap-to-band recombination.

If a sufficiently high electric field exists within a device, local band bending may be sufficient to allow electrons to tunnel, by internal field emission, from the valence band into the conduction band [62]. Therefore, the band-to-band tunneling effect is also included in our simulation. In the same manner, in a strong field, electrons can tunnel through the bandgap via trap states; thus, trap-assisted tunneling is also included. Finally, in any space charge region with a sufficiently high field, free carriers will acquire

sufficient energy to generate more free carriers when they collide with atoms of the crystal. This is the avalanche effect, and it is included in the simulation using the impact ionization model.

Fig. 4.1 shows the Atlas-software-determined variation of dark current with anode-to-cathode voltage for the PCSS shown in Fig. 3.8. The peak current shown in Fig. 4.1(a) occurs at 0.05 volts, or 5.0 kV/cm. This point and the ensuing negative differential resistance seen at higher voltages (electric fields) correlate, respectively and as expected, with the peak and region of negative differential mobility observed in the field-dependent behavior of electron drift velocities in GaAs, shown in Fig. 3.4. The approximately 4.3 pA constant anode current observed for voltages above approximately 0.3 volts or 30.0 kV/cm corresponds to the region where carriers are at their thermally limited constant saturation velocities [39]. Fig. 4.1(b) shows the onset of avalanche breakdown at approximately 7.0 volts, or 700.0 kV/cm, which is much higher than the bulk breakdown field in GaAs, shown in Table 2.1. This gives us another benefit of the narrow PCSS device width (0.1 um) besides a fast sweep-out charge removal time, as explained below.

Fig. 4.2 shows the PCSS current-electric field characteristics of PCSS devices with different device widths. As can be seen, the breakdown field is independent of device width and equal to the accepted value of approximately 300 kV/cm in GaAs for device widths greater than approximately 1.0 μm. As the PCSS device width becomes smaller than 1.0 μm, however, the breakdown field increases rapidly to approximately twice the accepted value in the 0.1 μm device of interest. This result is presumably due to the decreasing likelihood of the occurrence of the collisions needed to initiate the avalanche process as the switch width approaches the mean free path between

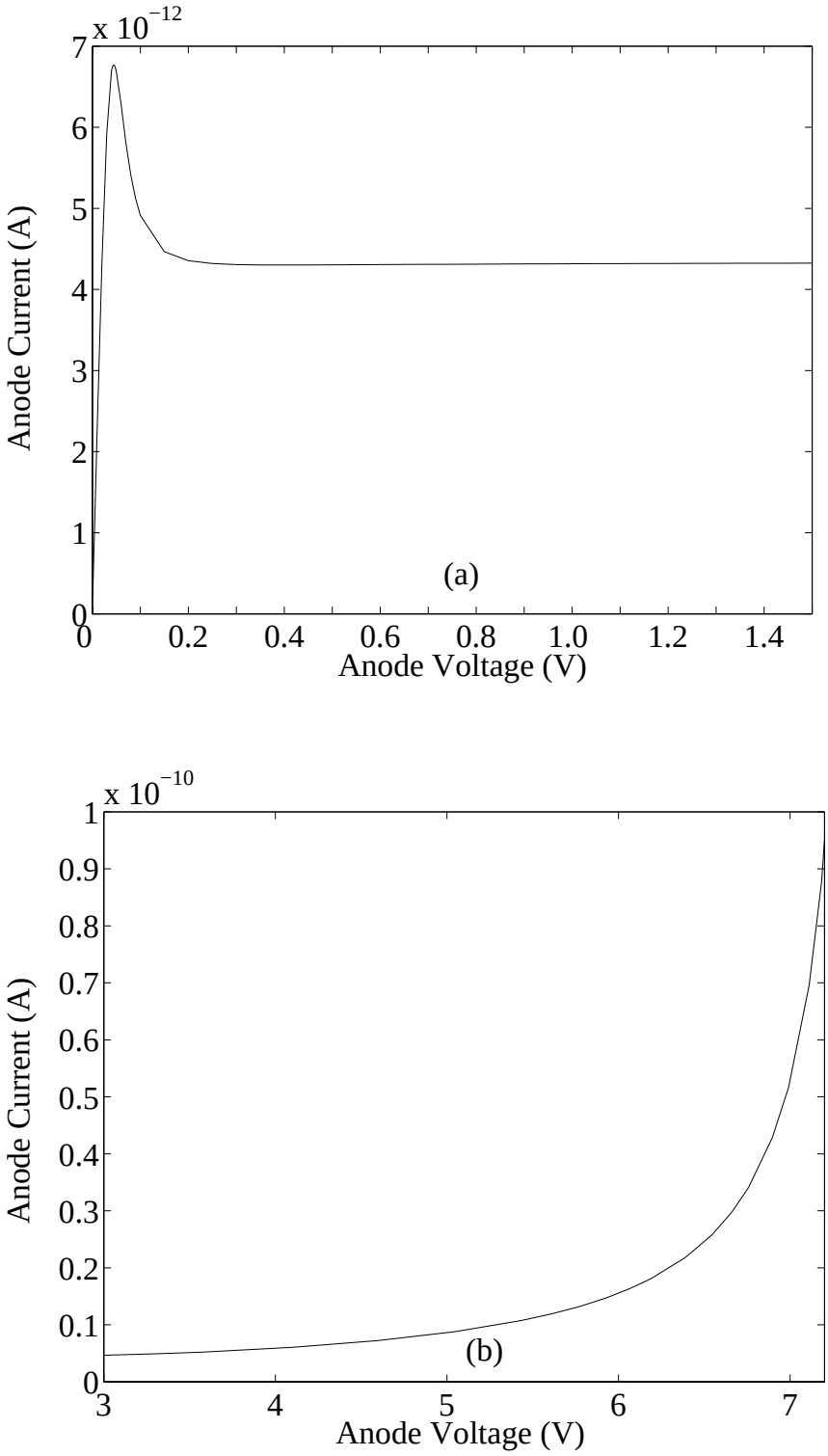

Fig. 4.1 Dark (no illumination) I-V data for the PCSS, showing: (a) negative differential resistance between 0.05 and 0.2 volts, (b) avalanche breakdown above approximately 7.0 volts.

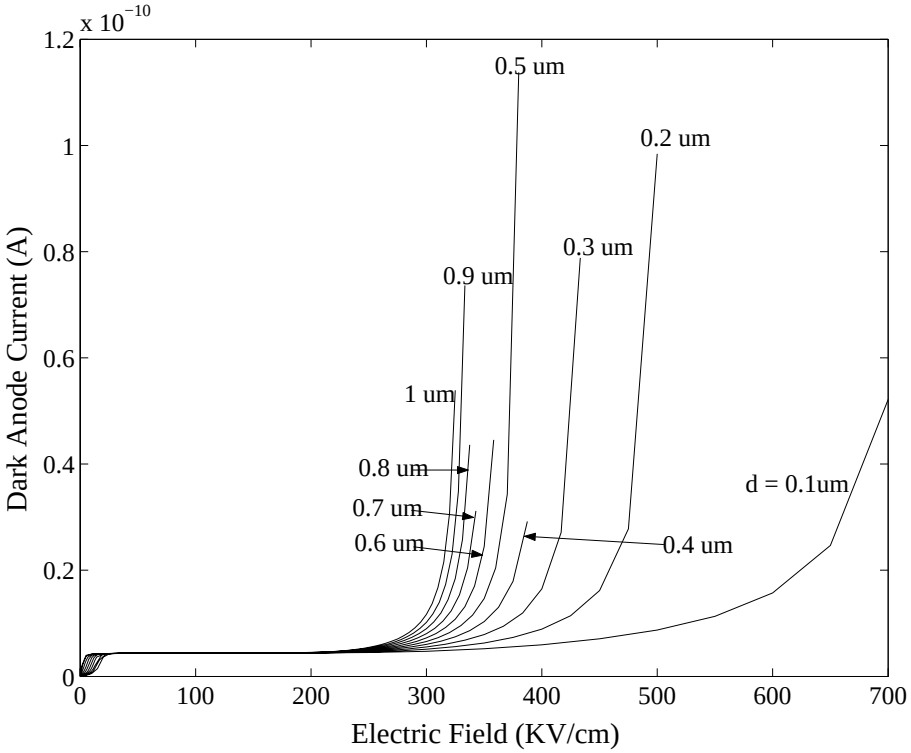

Fig. 4.2 PCSS current-electric field characteristics, illustrating the increase in breakdown field with decreasing device width.

collisions, which is approximately 0.1 um [27]. The significance of this result is that amplifier output power is proportional to photocurrent, which in turn increases with voltage across the PCSS. The larger breakdown fields shown in Fig. 4.2 mean that larger voltages can be placed across the switch before prohibitive avalanche occurs.

4.2 Intrinsic GaAs PCSS photoconductive performance

To study the photoconductive behavior of the switch, Mixedmode software was used to simulate its behavior in the simple amplifier circuit shown in Fig. 4.3. Note that this is just the upper branch of our new OE Class AB PA shown in Fig. 2.4 and 3.14. As

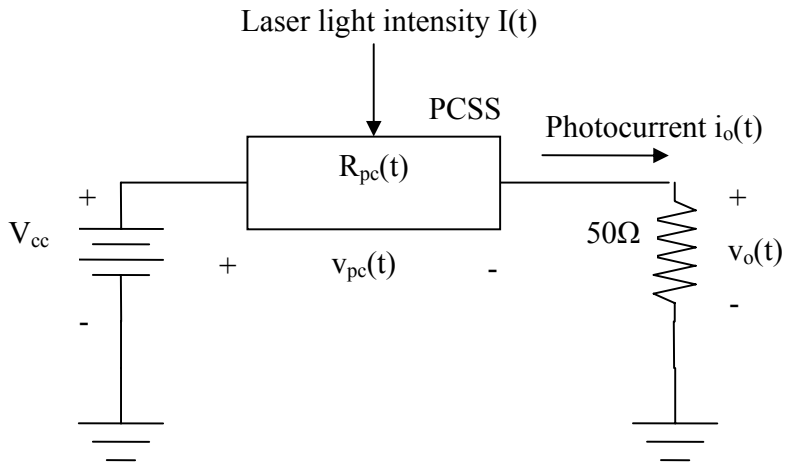

Fig. 4.3 Circuit used in the Mixedmode software program to study the photoconductive behavior of the PCSS.

shown in Fig. 3.8, the entire upper surface of the switch was assumed to be uniformly illuminated with 0.85 μm wavelength (1.45 eV photon energy) light to stimulate photoconductivity via band-to-band absorption. As shown in Fig. 4.4, the light was applied as a train of triangular pulses 50.0 ps wide and 100 ps apart or, equivalently, at a pulse rate of 10^{10} per second (10.0 GHz). The triangular pulses were used to approximate the DC-offset half-sinusoids that are produced by a laser modulator, but which are difficult to simulate with the Silvaco software. Furthermore, it is easier to observe the device turn-off delay time by using triangular pulses than other waveforms. The peak intensity of the optical pulses was assumed to be 4.0 x 10^7 W/cm^2, so that, considering the 0.1 μm by 3.0 μm device illumination area, the peak incident optical power was 0.12 W. Laser diodes that emit this level of power at 0.85 μm wavelength are commercially available [63]. The objective of the circuit illustrated in Fig. 4.3 is to produce a photocurrent $i_o(t)$ that in turn produces an output voltage $v_o(t)$ which replicates the temporal intensity shape of the laser pulse train (triangular here) and which is as large as

possible. The capability of the circuit to do this was evaluated as a function of the dc bias voltage V_{cc}.

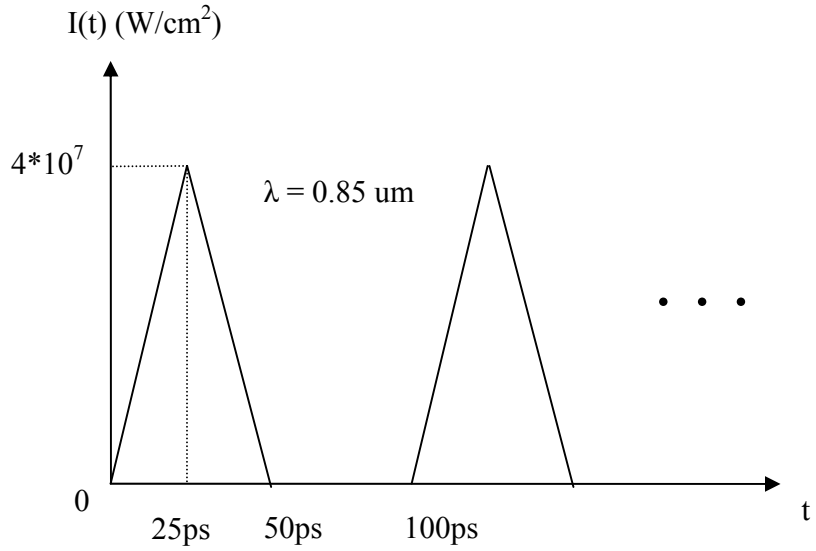

Fig. 4.4 Triangular laser pulse train used to study the PCSS.

Fig. 4.5 shows the temporal evolution of the photocurrent $i_o(t)$ in Fig. 4.3 resulting from light pulses of the type described above with the voltage V_{cc} in Fig. 4.3 set in turn to 0.5 V, 1.0 V, 2.0 V, 3.0 V, 4.0 V, 5.0 V, 6.0 V and 7.0 V. These curves illustrate an important performance tradeoff. As can be seen, the output photocurrent tends to follow the input triangular optical signal better as the bias voltage increases, but for values greater than approximately 5.0 V, the recovery time of the photocurrent begins to increase significantly beyond the 50.0 ps point required for 10.0 GHz operation, as the expanded curves in Fig 4.5(b) clearly show. This is due to the onset of avalanche, which, as Fig. 4.1(b) shows, begins to occur at approximately 500 kV/cm or 5.0 volts in a 0.1 μm wide device. This will be seen in later section to cause significant distortion in the output of the OE Class AB amplifier. On the other hand, for the low bias voltages the photocurrent

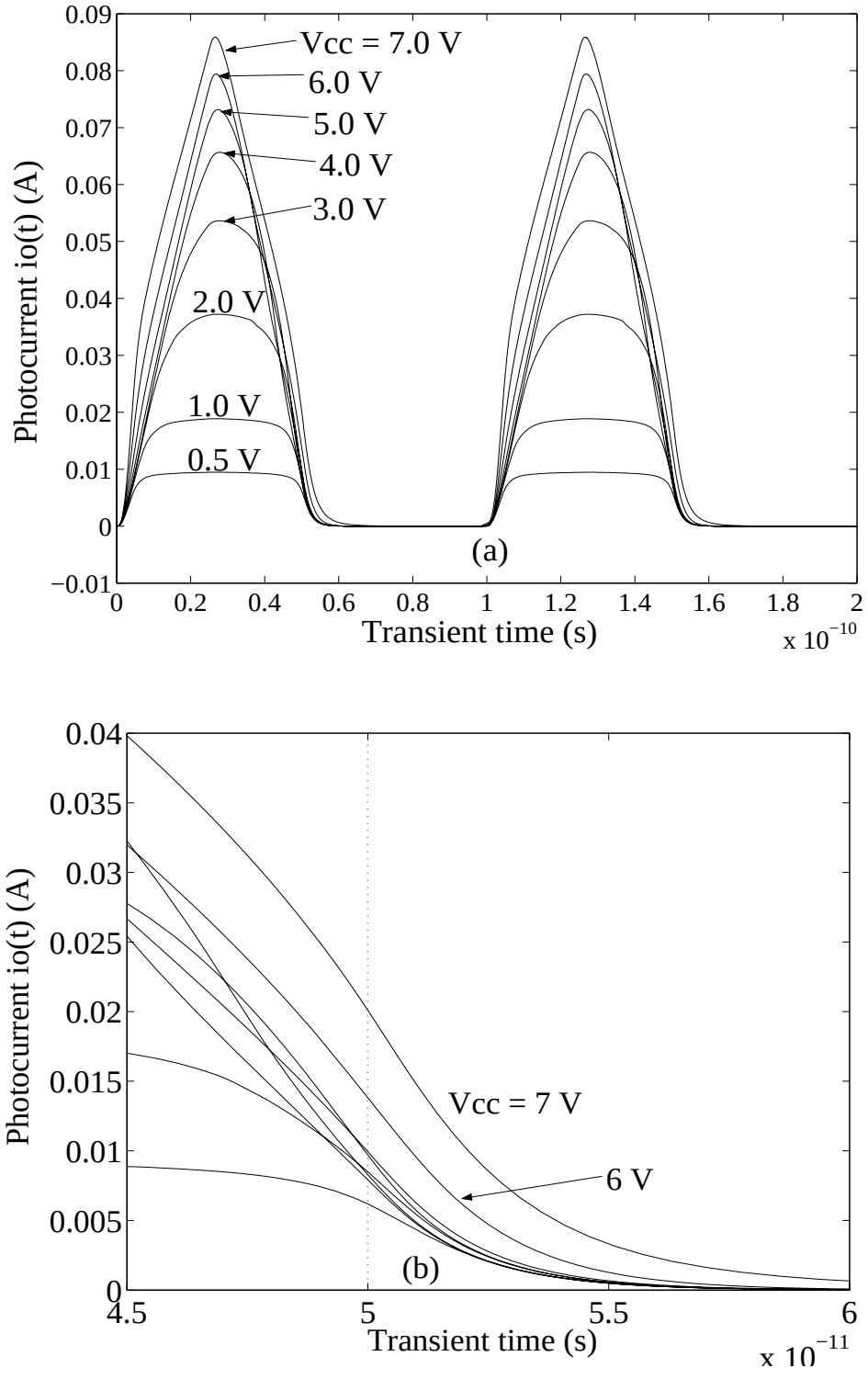

Fig. 4.5 Photocurrent $i_o(t)$ in Fig. 4.3: (a) output due to two laser pulses of the type shown in Fig. 4.4, with V_{cc} set to seven different values, (b) expansion of the data shown in Fig. 4.5(a) between $4.5*10^{-11}$ and $6.0*10^{-11}$ s.

decays to approximately zero in the 50.0 ps required for 10.0 GHz operation, probably because there is little or no avalanche at those low voltages, but as can be seen in Fig. 4.5(a), it loses its triangular shape and becomes flatter and more square wave-like as the bias voltage gets smaller. This is probably due to the current limiting effect of the 50 ohms resistor in Fig. 4.3. This is discussed in greater detail in Section 4.3.

Fig. 4.6 shows the electron and hole concentrations at several timer from zero to 60 ps throughout the transient for the V_{cc} = 2 volt data in Fig. 4.5. As can be seen, the electron and hole concentrations reach their maxima when the optical intensity is at its peak. When the optical pulse ends at 50 ps, there are still some residual electrons and

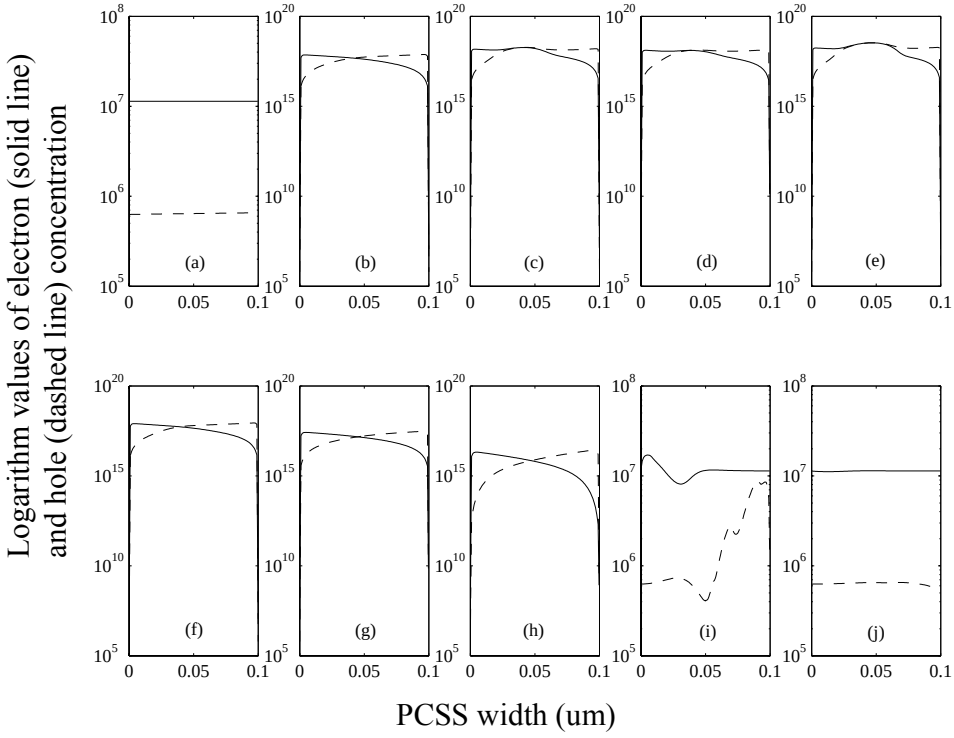

Fig. 4.6 Electron and hole concentration corresponding to Fig. 4.5 with V_{cc} set to 2 Volts, and the transient time equal to, (a) dark (before illumination), (b) 10 ps, (c) 20 ps, (d) peak (25 ps), (e) 30 ps, (f) 40 ps, (g) 45 ps, (h) 50 ps, (i) 55 ps, (j) 60 ps, (left side: anode, right side: cathode).

holes inside the PCSS device, as shown in Fig. 4.6(h). Fig. 4.6(i) shows that at 55 ps, most of the electrons are swept out and the electron concentration is near dark equilibrium value, shown in Fig. 4.6(a). However, since the holes are generally move slower than electrons, they take longer (60 ps) to completely sweep out, as shown in Fig. 4.6(j).

To illustrate the importance of the width of the photoswitch, Fig. 4.7 shows test circuit photocurrents due to a single light pulse of the type described above with PCSSs of different widths between 0.1 μm and 1.0 μm. In each case the bias voltage was adjusted to maintain the electric field across the device at 200 kV/cm, which is well below the threshold for avalanche breakdown, and the optical power in the incident laser pulse was

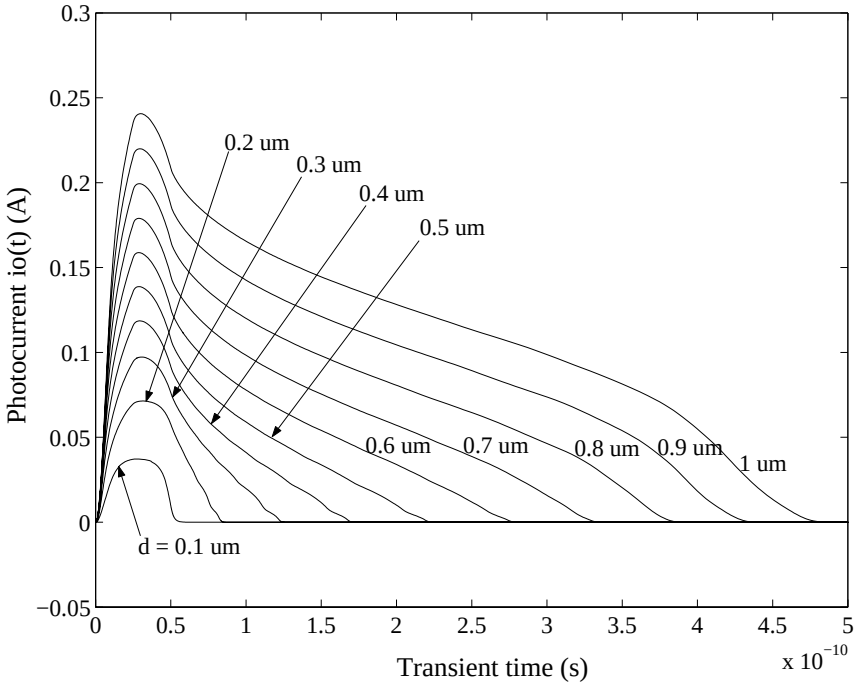

Fig. 4.7 Test circuit photocurrents due to a single 50.0 ps-wide triangular optical pulse, with PCSSs of different widths. Device electric field = 200 KV/cm and peak optical intensity = 4.0 x 10^7 W/cm^2.

adjusted to maintain the peak intensity at 4.0 x 10^7 W/cm^2, as in Fig. 4.4. The data in Fig. 4.7 shows that although the peak photocurrent increases linearly with device width, the signal is approximately able to track the 50.0 ps light pulse, which is essential for 10.0 GHz operation, only in the 0.1 μm wide device. The prohibitively increasingly longer photocurrent decay times in the wider photoswitches are due to an increase in sweep-out times resulting from greater distances between the electrodes, and a reduction of electron velocities from high collision-less ballistic values in the 0.1 μm wide device (0.7 um is approximately the mean free path between collisions) to lower saturated drift velocities determined by electron-lattice collisions in wider devices. Thus, for 10.0 GHz operation, it is necessary to sacrifice the gain evident in the wider devices for the required turn-off speed.

Fig. 4.8 shows the electron and hole concentrations corresponding to Fig. 4.7 when transient time is at 100 ps. As can be seen, at 100 ps, there are still relatively large carrier concentrations for the devices with widths greater than 0.2 um. This result shows just how critical the electrode separation is. The drastic difference in the photocurrent turn-off time may in part be due to the occurrence of ballistic transport in the 0.1 um device because 0.1 um happens to be the mean free path (mfp) between electron collisions.

Fig. 4.9 shows the results of a parametric study of the PCSS device height. While maintaining the same width and depth of our PCSS device, 0.1 um and 3 um, respectively, and with bias voltage V_{cc} of 4 V, we varied the PCSS height from 1 um to 10 um. The simulation results indicate that when the PCSS height is smaller than 4 um, the photocurrent $i_o(t)$ decreases dramatically because an increasing amount optical energy cannot be absorbed by GaAs due to the absorption coefficient, as shown in Equation (3.5).

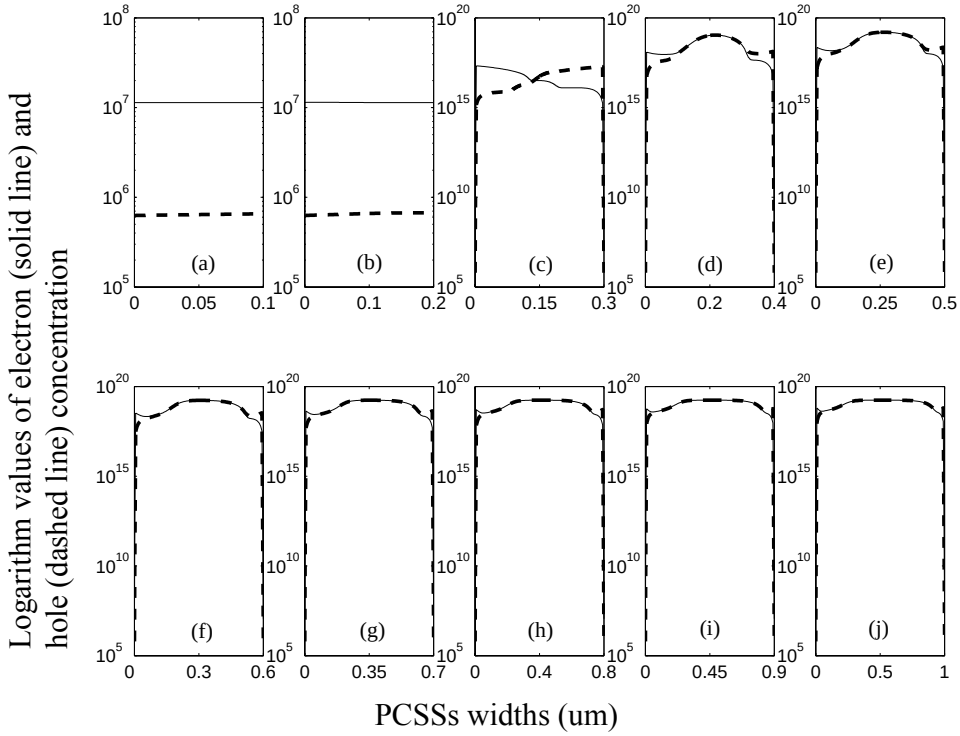

Fig. 4.8 Electron and hole concentrations 100 ps into the transient for the data shown in Fig. 4.7. (a) 0.1 um, (b) 0.2 um, (c) 0.3 um, (d) 0.4 um, (e) 0.5 um, (f) 0.6 um, (g) 0.7 um, (h) 0.8 um, (i) 0.9 um, (j) 1.0 um. (left side: anode, right side: cathode)

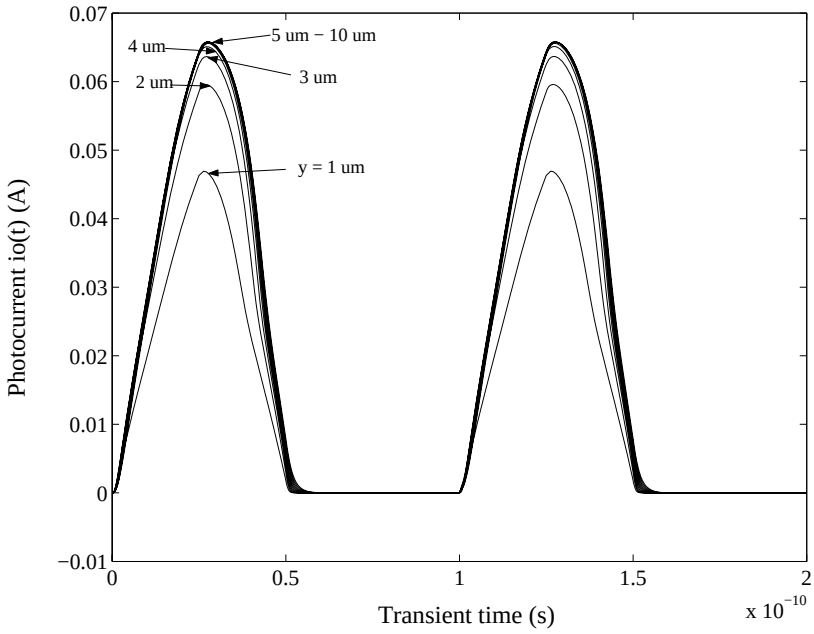

Fig. 4.9 Test circuit photocurrents for PCSS devices with heights varied from 1 um to 10 um. The width and depth of the PCSS device are 0.1 um and 3 um, respectively, with bias voltage V_{cc} of 4 V.

Changes in photocurrent become insignificant when the PCSS height equals 5 um or more because most of the optical energy has been absorbed by the GaAs PCSS device.

4.3 Discussion of simulation results

To quantitatively interpret the data in Fig. 4.5, note in Fig. 4.3 that as the laser light is absorbed by the PCSS, its diminishing resistance $R_{pc}(t)$ determines the photocurrent $i_o(t)$, the voltage $v_{pc}(t)$ across the PCSS, and the output voltage $v_o(t)$ through the equations

$$i_o(t) = V_{cc}/(R_{pc}(t) + 50) \qquad (4.1)$$

$$v_{pc}(t) = V_{cc} - 50i_o(t) \qquad (4.2)$$

and $$v_o(t) = 50i_o(t). \qquad (4.3)$$

As the light pulse increases in intensity from zero to its maximum value (4.0×10^7 W/cm^2) and returns to zero, the switch resistance decreases from a very large off-state value $R_{pc}(max)$ to a minimum value $R_{pc}(min)$ and returns to $R_{pc}(max)$. Simultaneously, photocurrent $i_o(t)$ increases, as shown in Fig. 4.5 and according to Equation (4.1), to a maximum $i_o(max)$ and returns to zero. Given $i_o(max)$ from the simulation data, Equation (4.1) gives $R_{pc}(min)$ as

$$R_{pc}(min) = [V_{cc} - 50i_o(max)]/i_o(max). \qquad (4.4)$$

Equations (4.2) and (4.3) show, respectively, that while the photocurrent rises and falls, the switch voltage falls and rises, reaching a minimum value $v_{pc}(min)$ given by

$$v_{pc}(min) = V_{cc} - 50i_o(max) \qquad (4.5)$$

and the output voltage rises and falls, reaching its maximum value $v_o(max)$ when the photocurrent is maximum, i.e.,

$$v_o(max) = 50i_o(max) \qquad (4.6)$$

The second, third, and fourth columns of Table 4.1 list, for each of the values of V_{cc} considered in the simulations and given in the first column, the peak photocurrent from Fig. 4.5(a) and the corresponding values of $R_{pc}(min)$ and $v_{pc}(min)$ as determined with Equations (4.4) and (4.5), respectively. The sixth column in the table lists the corresponding ratios of $v_o(max)$ to V_{cc}, where $v_o(max)$ in the fifth column is determined with Equation (4.6). This quantity represents the peak efficiency of the PCSS in converting dc voltage to amplified signal (light intensity) voltage at the load. The final two columns in Table 4.1 contain the maximum and minimum values of electric field across the switch, E(max) and E(min), associated with, respectively, the corresponding values of V_{cc} ($v_{pc}(t)$ in the absence of illumination) and $v_{pc}(min)$ listed in the first and fourth columns. Note that for V_{cc} greater than 5.0 volts, E(max) is large enough to initiate avalanche breakdown and increase photocurrent recovery time, as discussed above.

The data in Fig. 4.5 and Table 4.1 show that there are performance tradeoffs of the amplifier/PCSS combination throughout the range of V_{cc} values considered. On one hand,

V_{CC} (Volts)	i_o (max) (Amps)	R_{pc} (min) (Ohms)	v_{pc} (min) (Volts)	v_o (max) (Volts)	v_o (max)/V_{cc}	E (max) (KV/cm)	E (min) (KV/cm)
0.5	0.0095	2.6	0.025	0.475	0.95	50	2.5
1	0.019	2.6	0.05	0.95	0.95	100	5.0
2	0.037	4.1	0.15	1.85	0.93	200	15.0
3	0.054	5.6	0.30	2.7	0.90	300	30.0
4	0.066	10.6	0.70	3.3	0.83	400	70.0
5	0.073	18.5	1.35	3.65	0.73	500	135
6	0.079	25.9	2.05	3.95	0.66	600	205
7	0.086	31.4	2.70	4.3	0.61	700	270

Table 4.1 Characteristics of the PCSS as V_{cc} in Fig. 4.3 is varied.

the peak efficiency of the circuit (the sixth column in Table 4.1) is quite high and relatively constant for V_{cc} values below approximately 3.0 volts, but decreases rather rapidly as V_{cc} increases beyond 3.0 volts. On the other hand, the photocurrents shown in Fig. 4.5 are approximately triangular, i.e., undistorted, for the larger V_{cc} values where circuit efficiency is relatively low, but they become increasingly rounded and flattened at the small V_{cc} values where the efficiency is high.

The reduction in circuit efficiency as V_{cc} gets larger and the photocurrent duplicates the shape of the laser pulse intensity with less and less distortion can be explained in terms of the electric-field-dependent behavior of electron drift velocity in GaAs, illustrated in Fig. 3.4. Since electron mobility is so much greater than hole mobility in GaAs, the variation of the electrical resistivity $\rho(t)$ (in ohm-cm) of the material during illumination by the laser pulse can be approximated as

$$\rho(t) = [qn(t)\mu_n(t)]^{-1} \qquad (4.7)$$

where q is the electron charge, n(t) is the concentration of photoelectrons, and $\mu_n(t)$ is their mobility. Assuming that the laser intensity is small enough throughout the entire pulse that the quantum efficiency for photocarrier generation is constant, n(t) essentially follows the laser pulse intensity I(t), having a value n(max) at the peak of the laser pulse. Thus, equation (4.7) indicates that $\rho(t)$ is minimum with value $\rho(min)$ at the peak of the pulse. Assuming also that n(t) is never large enough to affect carrier mobility through carrier-carrier scattering, $\mu_n(t)$ depends only on the instantaneous electric field and carrier drift velocity through the relationship

$$\mu_n(t) = v_d(t)/E(t) \qquad (4.8)$$

As can be seen in Table 4.1, for V_{cc} greater than or equal to 2.0 volts, the electric field across the switch is always at least 15.0 kV/cm, so that, as shown in Fig. 3.3, electron drift velocities are constant at the thermally limited saturation value v_{sat}. Thus, Equation (4.8) becomes

$$\mu_n(t) = v_{sat}/E(t) \qquad (4.9)$$

and the carrier mobility varies inversely with the electric field during application of the laser pulse, reaching a maximum value $\mu_n(max)$ when E(t) is minimum at the peak of the laser pulse. Since E(min) increases with V_{cc}, $\mu_n(max)$ decreases accordingly. Thus, at the peak of the laser pulse Equation (4.7) can be written as

$$\rho(min) = [qn(max)\mu_n(max)]^{-1} \qquad (4.10)$$

If n(max) is relatively independent of V_{cc} when $v_d = v_{sat}$ and $\mu_n(max)$ decreases with V_{cc}, it is clear from Equation (4.10) that $\rho(min)$ and thus $R_{pc}(min)$ increase with V_{cc} when $v_d = v_{sat}$, causing peak efficiency $v_o(max)/V_{cc}$ to drop, as shown in the table.

When V_{cc} is relatively small, i.e., 0.5 and 1.0 volts in Table 4.1, E(min) lies approximately in the linear portion of the v_d versus E data shown in Fig. 3.4, where the electron mobility is roughly constant and much larger than it is when $v_d = v_{sat}$, as discussed above. Thus $\mu_n(max)$ is independent of V_{cc} and much larger than in the saturated drift velocity case, and Equation (4.10) shows that $\rho(min)$ and thus $R_{pc}(min)$ are approximately constant and much smaller than in the saturated case, resulting in large and constant peak efficiencies, as verified by the data in the table.

The rounding and flattening of the photocurrents shown in Fig. 4.5 when V_{cc} is small and circuit efficiency is high can be explained in terms of the current limiting behavior of the 50 ohm load. In the ideal case of zero minimum PCSS resistance during

illumination, Fig. 4.3 shows that the peak photocurrent i_o(max) would be equal to V_{cc}/50. At the larger V_{cc} values, V_{cc}/50 is significantly larger than the corresponding i_o(max) given in Table 4.1, suggesting that the circuit has little effect on the photocurrent, allowing it to follow the temporal shape of I(t), as is the case in Fig. 4.5. At smaller values of V_{cc}, V_{cc}/50 approaches i_o(max) given in Table 4.1, suggesting a growing current limiting role by the circuit. At the smallest V_{cc} values, V_{cc}/50 and i_o(max) are nearly identical, suggesting a strong current limiting role by the circuit. The extensive distortion seen in the low V_{cc} traces in Fig. 4.5 support this.

The 0.1 um device data in Fig. 4.5 and Table 4.1 show that there is an optimum range of V_{cc} values, between approximately 3.0 and 5.0 volts, for which the device efficiency is reasonably high and the photocurrent is relatively undistorted, either by circuit current limiting or by the onset of avalanche. The largest peak output voltage in that window is 3.65 volts, corresponding to a peak output power of approximately 0.27 Watts. To try to improve this result, simulations were performed on a multi-layer PCSS device which we will discuss in Section 4.5.

4.4 OE Class AB push-pull PA performance

Mixedmode software simulations were then performed with the new PCSS in the OE Class AB push-pull power amplifier discussed in Chapter 3 and shown again in Fig. 4.10. The output matching network shown in Fig. 3.13 is omitted from Fig. 4.10 because the Mixedmode software assumes that the circuit is well matched. Note that the amplifier in Fig. 4.10 is just an expansion of the amplifier of Fig. 4.3 needed to produce the

negative half-cycle of the required 10 GHz sinusoid. The optical pulse trains indicated in Fig. 4.10 are identical to that in Fig. 4.4 with the exception that the pulse train illuminating PCSS2 is delayed by one-half cycle or 50 ps with respect to the pulse train illuminating PCSS1.

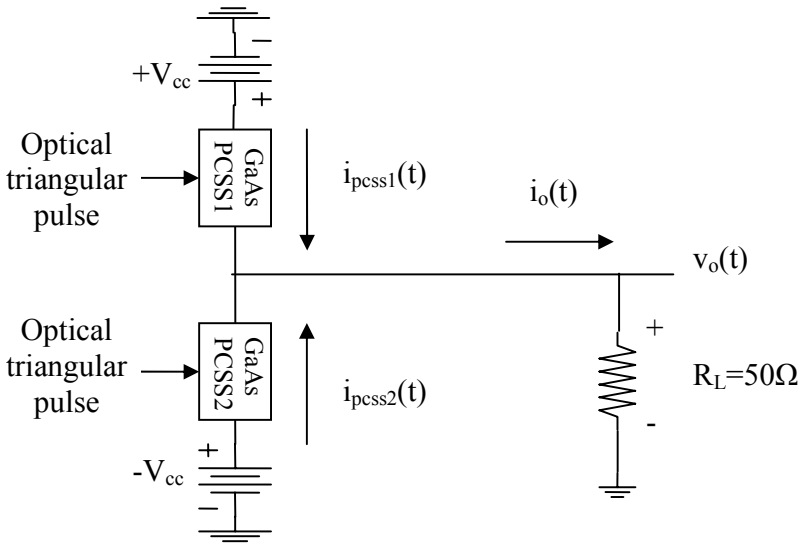

Fig. 4.10 OE Class AB push-pull microwave PA with PCSSs.

The output and input power calculations of Chapter 3 were based on half-sinusoidal optical pulse trains. Here, we derive the output and input powers associated with triangular pulse trains. Fig. 4.11(a) shows the ideal output waveform of the PA in Fig. 4.10 with half-triangular optical pulse train inputs. The instantaneous output power can be written as

$$p_o(t) = v_o(t) * i_o(t) = v_o(t) * \frac{v_o(t)}{R_L} = \frac{v_o^{\,2}(t)}{R_L}. \quad (4.11)$$

The waveform of $v_o^2(t)$ is shown in Fig. 4.11(b). From Equation (4.11), the average output power P_o can be calculated as

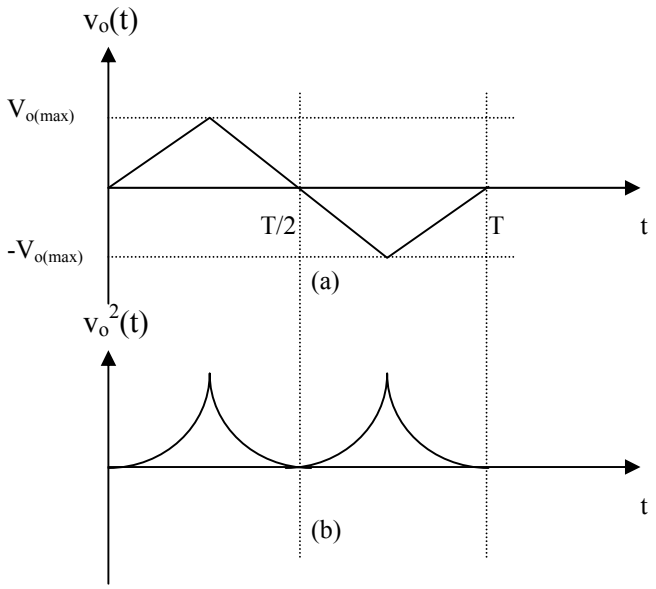

Fig. 4.11 (a) Ideal output voltage waveform of our simulated OE Class AB push-pull microwave PA, (b) waveform of $v_o^2(t)$.

$$P_o = \frac{1}{T}\int p_o(t)dt = \frac{1}{R_L}\frac{1}{T/2}\int_0^{T/2} v_o^{\,2}(t)dt \qquad (4.12)$$

where $\frac{1}{T/2}\int_0^{T/2} v_o^{\,2}(t)dt$ is the mean of the square of the triangular voltage waveform, which is $\frac{V_{o(max)}^{\,2}}{3}$ [64]. Therefore,

$$P_o = \frac{V_{o(max)}^{\,2}}{3R_L}. \qquad (4.13)$$

At the input, the average power for one dc supply is equal to

$$P_{s+} = 1/T \int_0^{T/2} V_{cc} * i_{pcss1}(t)dt$$

$$= 1/T \int_0^{T/2} V_{cc} * \frac{v_o(t)}{R_L}dt$$

$$= \frac{V_{cc}}{T * R_L} \int_0^{T/2} v_o(t)dt \qquad (4.14)$$

where $\int_0^{T/2} v_o(t)dt$ is the area of the triangular waveform; thus,

$$P_{s+} = \frac{V_{cc}}{T * R_L} * \frac{\frac{T}{2} * V_{o(\max)}}{2}$$

$$= \frac{V_{cc} * V_{o(\max)}}{4R_L}. \qquad (4.15)$$

Therefore, for two dc supplies

$$P_s = \frac{V_{cc} * V_{o(\max)}}{2R_L}. \qquad (4.16)$$

The efficiency of the circuit is, therefore,

$$\eta = P_o / P_s = \frac{2V_{o(\max)}}{3V_{cc}}. \qquad (4.17)$$

The maximum efficiency will occur when the resistance of the PCSS is zero (ideal case) in which case $V_{o(max)} = V_{cc}$; thus, the maximum efficiency for our simulated circuit is 66.7 %, which is smaller than the 78.5 % theoretical efficiency when sinusoidal optical waveforms are used, as shown in section 3.2.3.

Figure 4.12 shows the simulation results of the load voltage $v_o(t)$ in Fig. 4.10 resulting from half-triangular optical pulses with peak value of 0.12 W and average power of 0.06 W, with the voltage V_{cc} in Fig. 4.10 set in turn to 0.5 V, 1.0 V, 2.0 V, 3.0 V, 4.0 V, 5.0 V, 6.0 V and 7.0 V. The PCSS devices were 0.1 um wide. Similar to Fig. 4.5(a), the curves in Fig. 4.12 are flattened and rounded in the low bias voltage cases, where current limiting by the load is significant; they are increasingly distorted when the bias voltage is

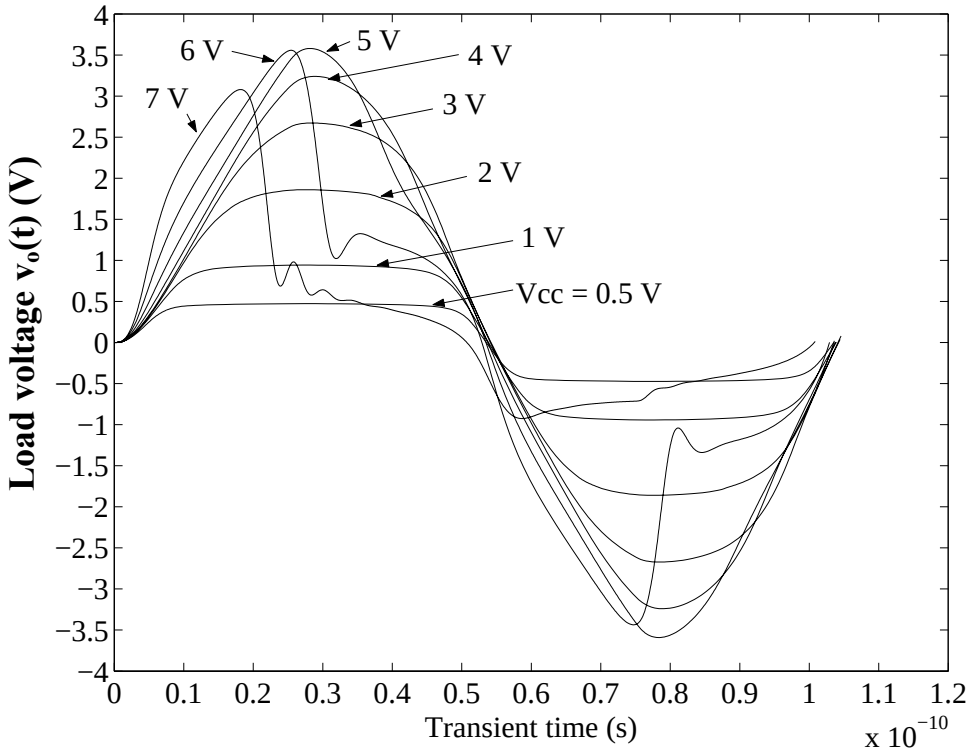

Fig. 4.12 Load voltage $v_o(t)$ in Fig. 4.10 with V_{cc} set to seven different values.

large enough to cause significant avalanche; and they are approximately triangular (the desired response) for a narrow range of bias voltages between approximately 3.0 V and 5.0 V.

Table 4.2 shows the important characteristics of the amplifier as a function of V_{cc} for the three cases in Fig. 4.12 for which the output voltage is reasonably triangular and

V_{CC} (Volts)	V_o(max) (Volts)	P_{opt} (Watts)	P_s (Watts)	P_o (Watts)	Efficiency (η,%)	Gain (dB)	PAE (%)
3	2.67	0.06	0.080	0.048	60.0	-1.9	N/A
4	3.24	0.06	0.13	0.070	53.8	1.3	3.2
5	3.58	0.06	0.18	0.085	47.5	3.0	14.0

Table 4.2 Characteristics of the OE Class AB push-pull PA as V_{cc} in Fig. 4.10 is varied from 3 to 5 Volts.

the equations for the triangular approximation can be applied. Equations (4.13) and (4.16) were used to find the output and input powers of the amplifier. The results are shown in the fourth and fifth column of Table 4.2, respectively. The sixth column shows that the resulting efficiency varies from 60.0 % to 47.5 %. The gain G of the circuit, given by

$$G = \frac{P_o}{P_{opt}}, \qquad (4.18)$$

is given in db (G(dB) = 20 log (G)) in the seventh column of Table 4.2. The negative gain observed when V_{cc} = 3 V occurs because Schottky contacts are used in the PCSS design to prevent electron injection and improve device speed, which decreases the gain of the PCSS. However, at V_{cc} = 5 V, a gain of 3 db is observed. The eighth column of Table 4.2 shows the power added efficiency (PAE) of the circuit, where PAE is defined as

$$PAE = \frac{(P_o - P_{opt})}{P_s}. \qquad (4.19)$$

With negative gain, of course, the PAE is negative; thus, the PAE value for that case is not given. Here, we idealize the insertion loss of the Mach-Zehnder beam modulator equals to zero which gives us equal amount of the modulated output optical power, P_{opt}, and input microwave power of the modulator. In practice, the circuit PAE value will be reduced due to the insertion loss of the optical modulator [65].

In order to examine the influence of peak optical intensity on the results, simulations were performed with the peak optical intensity equal to 5.0 x 10^7 W/cm^2 and 3.0 x 10^7 W/cm^2. The results are shown in Fig 4.13 and Table 4.3 for the higher intensity case and in Fig. 4.14 and Table 4.4 for the lower intensity case. The load voltage plots show that signal distortion gets worse when optical intensity increases and it gets better

when the optical intensity decreases. The results reflect the fact that higher optical intensities create more seed charge to participate in avalanche. Thus the signal distortion gets worse and occurs at lower V_{cc} values as optical intensity increase. On the other hand, the higher intensities cause smaller minimum resistances of the PCSS devices, which leads to greater efficiency. This can be seen by comparing the efficiency values in Tables 4.2, 4.3, and 4.4 at V_{cc} = 4.0 volts, a value at which the output voltages in all three cases are reasonably undistorted. As the optical intensity increases, efficiency increases but the output voltage becomes increasingly distorted.

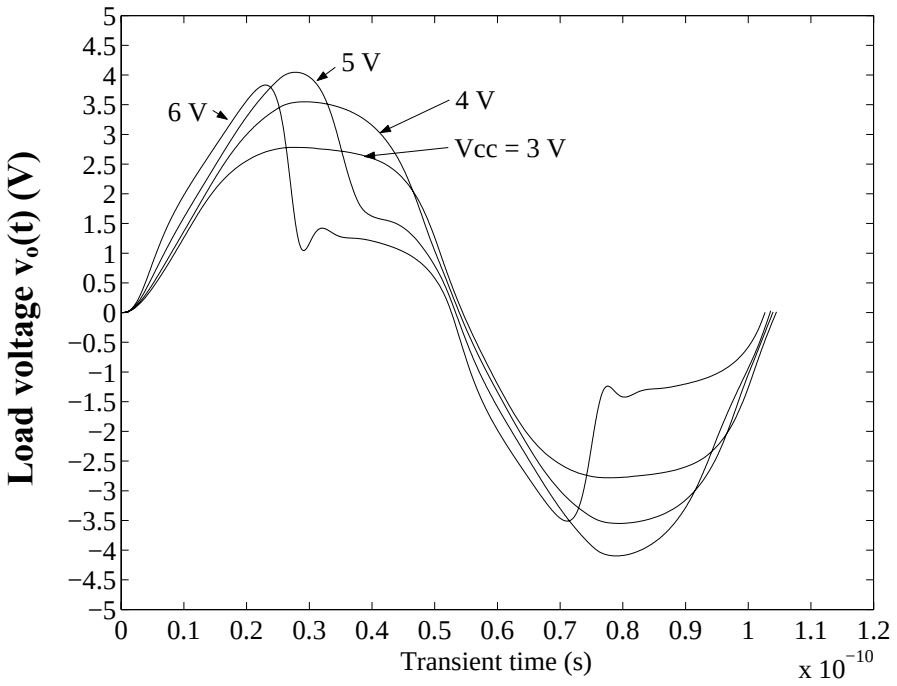

Fig. 4.13 Load voltage $v_o(t)$ in Fig. 4.10 when the peak optical intensity is $5*10^7$ W/cm^2.

V_{CC} (Volts)	V_o(max) (Volts)	P_{opt} (Watts)	P_s (Watts)	P_o (Watts)	Efficiency (η,%)	Gain (db)	PAE (%)
3	2.78	0.075	0.083	0.052	62.7	-2.5	N/A
4	3.55	0.075	0.14	0.084	60.0	1.0	6.4
5	4.00	0.075	0.20	0.105	52.5	2.9	15.0

Table 4.3 Characteristics of the OE Class AB push-pull PA with a peak optical intensity of $5*10^7$ W/cm^2.

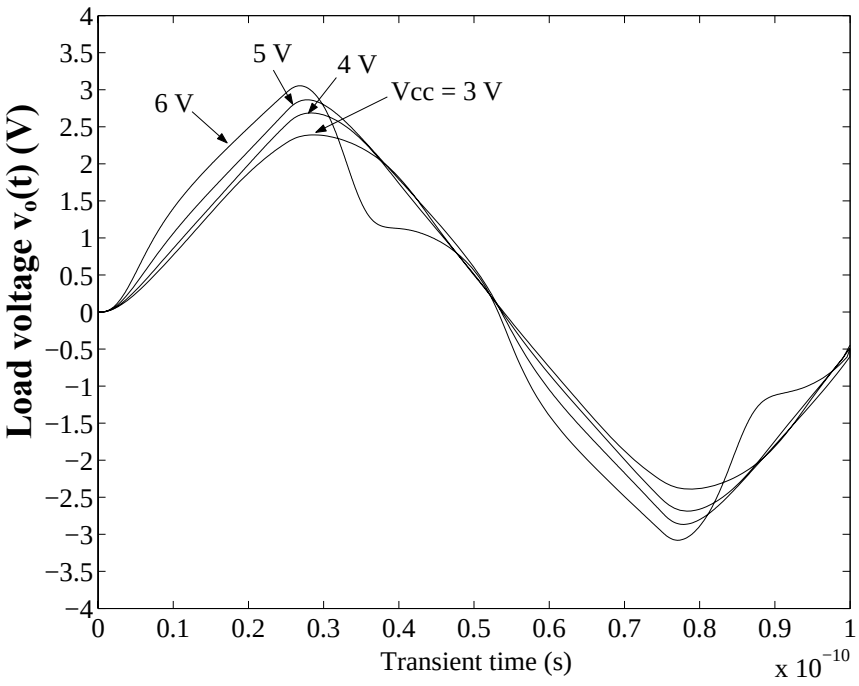

Fig. 4.14 Load voltage $v_o(t)$ in Fig. 4.10 when the peak optical intensity is $3*10^7$ W/cm^2.

V_{CC} (Volts)	V_o(max) (Volts)	P_{opt} (Watts)	P_s (Watts)	P_o (Watts)	Efficiency (η,%)	Gain (db)	PAE (%)
3	2.39	0.045	0.072	0.038	52.8	-1.5	N/A
4	2.69	0.045	0.11	0.048	43.6	0.6	2.7
5	2.86	0.045	0.14	0.055	39.3	1.7	7.1

Table 4.4 Characteristics of the OE Class AB push-pull PA with a peak optical intensity of $3*10^7$ W/cm^2.

4.5 OE Class AB push-pull PA with multi-layer PCSS structures

As discussed in the previous section, when embedded our novel intrinsic-GaAs PCSSs are used in the OE Class AB push-pull PA circuit, an optimum, intermediate value of the bias voltage V_{cc} can be identified for which the amplifier is more than 50.0 % efficient and produces 85 mW output power with very little distortion at 10 GHz. In order to increase the output power, our PCSS device needs to be able to sustain higher V_{cc} bias voltage. If we increase the width, d, of the PCSS (electrode distance), as shown in Fig. 3.8, to increase the bias voltage, our analysis shows that the trade off of increasing d would be the increase of the sweep-out time and the decrease of the breakdown field of the device, as shown in Fig. 4.7 and Fig. 4.2, respectively. Alternatively, we could stack several PCSS devices together in one multi-layer structure, in which, as discussed in Section 3.3, higher output power levels can be expected without sacrificing the sweep-out time and breakdown field of the device.

Fig. 4.15 shows the Mixedmode simulation result of the photocurrent $i_o(t)$ in Fig. 4.3 by using a two-layer intrinsic GaAs PCSS structure, as shown in Fig. 3.18. The

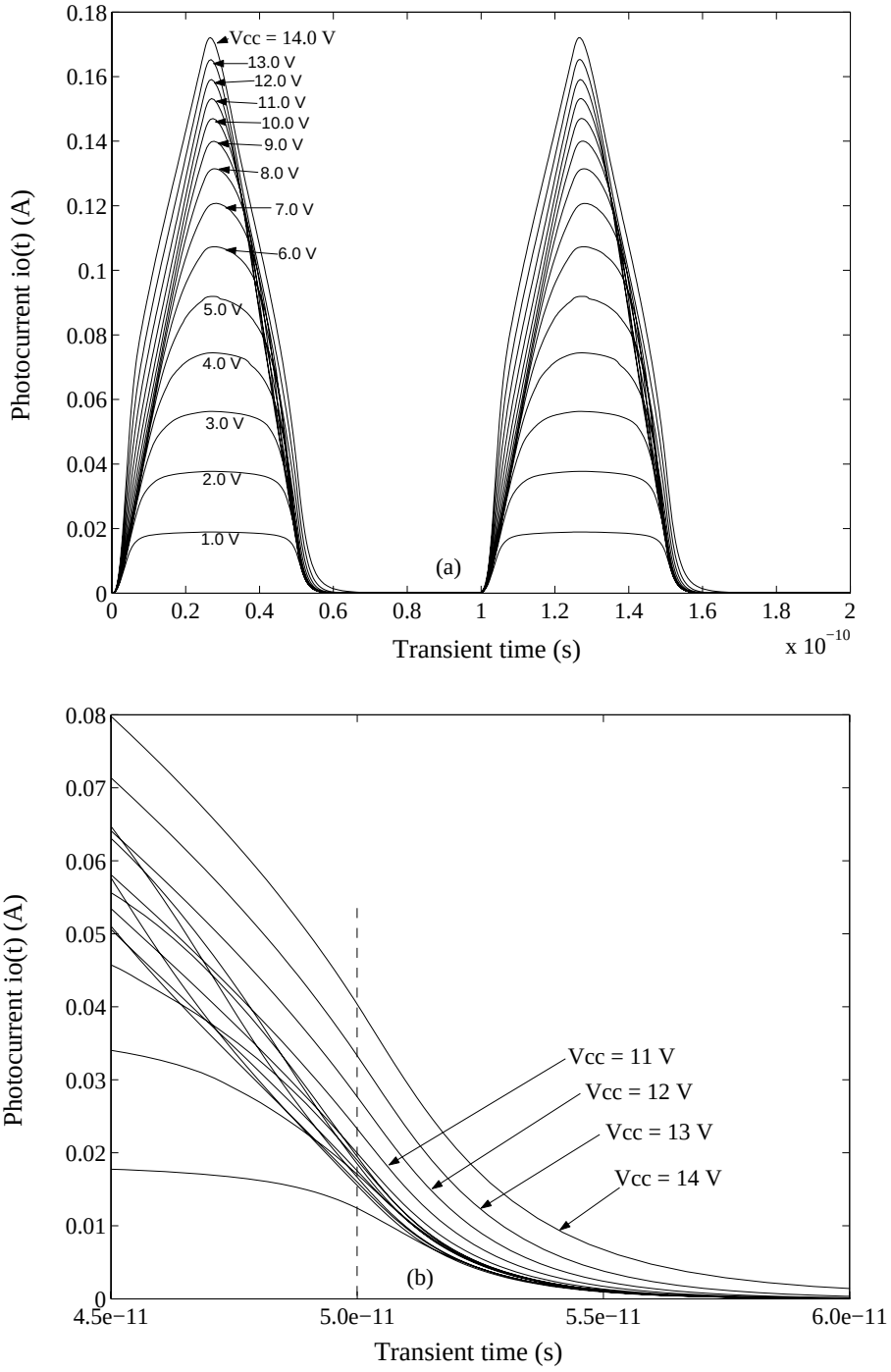

Fig. 4.15 Photocurrent $i_o(t)$ in Fig. 4.3 due to a two-layer intrinsic GaAs PCSS structure as shown in Fig. 3.18: (a) output due to two laser pulses of the type shown in Fig. 4.4, with V_{cc} set to fourteen different values, (b) expansion of the data shown in Fig. 4.15(a) between $4.5*10^{-11}$ and $6.0*10^{-11}$ s.

photocurrent $i_o(t)$ is due to a triangular pulse train, as shown in Fig. 4.4, with the voltage V_{cc} in Fig. 4.3 set in turn to 1 V to 14 V in increments of 1 V. In order to eliminate the series resistance problem, the depth of the device was set to 6 um, as discussed in Section 3.3. For our two-layer device, we can successfully increase the V_{cc} to 14 V, which corresponds to 700 KV/cm, which is the breakdown field of a single layer device. Furthermore, the simulation results show the same trade-offs as discussed in Section 4.2. The output photocurrent tends to follow the input triangular optical signal better as the bias voltage increases, but for values greater than approximately 10.0 V, the sweep-out time of the photocurrent begins to increase significantly beyond the 50.0 ps point required for 10.0 GHz operation, as the expanded curves in Fig 4.15(b) clearly show. This is again due to the onset of avalanche, which, as Fig. 4.1(b) shows, begins to occur at approximately 500 kV/cm or 10.0 volts in a 0.2 μm wide device. On the other hand, for the lower bias voltages, below approximately 6 V, the photocurrent loses its triangular shape and becomes flatter and more square wave-like due to the current limiting role of the load.

Table 4.5 shows the characteristics of a two-layer PCSS structure as V_{cc} in Fig. 4.15 is varied. Comparing it with the single layer PCSS case, summarized in Table 4.1, the minimum PCSS resistance values, R_{pc} (min), listed in the third column of each table agree with each other when both maximum electric fields across the device, E (max), listed in the seventh column, are equal. For example, if E (max) equals 500 KV/cm, R_{pc} (min) for a single layer PCSS is 18.50 ohms while R_{pc} (min) for a two-layer PCSS is 18.03 ohms. Corresponding minimum resistance values for both cases also yield similar peak circuit efficiency listed in the sixth column. However, when E (max) equals 500 KV/cm,

V_{CC} (Volts)	i_o (max) (Amps)	R_{pc} (min) (Ohms)	v_{pc} (min) (Volts)	v_o (max) (Volts)	v_o (max)/V_{cc}	E (max) (KV/cm)	E (min) (KV/cm)
1	0.019	2.6	0.05	0.95	0.95	50	2.5
2	0.038	2.6	0.10	1.90	0.95	100	5.0
3	0.056	3.8	0.20	2.80	0.933	150	10.0
4	0.074	4.1	0.30	3.70	0.925	200	15.0
5	0.092	4.3	0.40	4.60	0.92	250	20.0
6	0.107	6.1	0.65	5.35	0.89	300	32.5
7	0.121	7.9	0.95	6.05	0.86	350	47.5
8	0.132	10.61	1.40	6.60	0.83	400	70.0
9	0.140	14.29	2.00	7.00	0.78	450	100.0
10	0.147	18.03	2.65	7.35	0.74	500	132.5
11	0.153	21.90	3.35	7.65	0.70	550	167.5
12	0.159	25.47	4.05	7.95	0.66	600	202.5
13	0.165	28.79	4.75	8.25	0.63	650	237.5
14	0.172	31.40	5.40	8.60	0.61	700	270.0

Table 4.5 Characteristics of a two-layer PCSS structure as V_{cc} in Fig. 4.15 is varied.

i_o (max) and v_o (max) increase from 0.073 A and 3.65 V, respectively, for a single layer PCSS to 0.147 A and 7.35 V, respectively, for a two-layer PCSS. The reason for this doubling of the circuit output current and voltage is that we are able to bias the two-layer PCSS device with twice higher source voltage, V_{cc}, while also maintaining the same minimum PCSS. This means higher output power can be expected with our two-layer PCSS structure

Figure 4.16 shows the simulation results for the OE Class AB push-pull microwave PA shown in Fig. 4.10 with our two-layer PCSSs. Results are shown for the bias voltage V_{cc} set in turn to 7.0 V, 8.0 V, 9.0 V, 10.0 V, 11.0 V, 12.0 V, 13.0 V and 14.0 V. The lower voltage cases are not shown here because of the current limiting problem shown in Fig. 4.15, which prevents the output voltage from replicating the input light pulse. From Fig. 4.16, we see that when the bias voltage is large enough to cause significant avalanche, the load voltage is increasingly distorted.

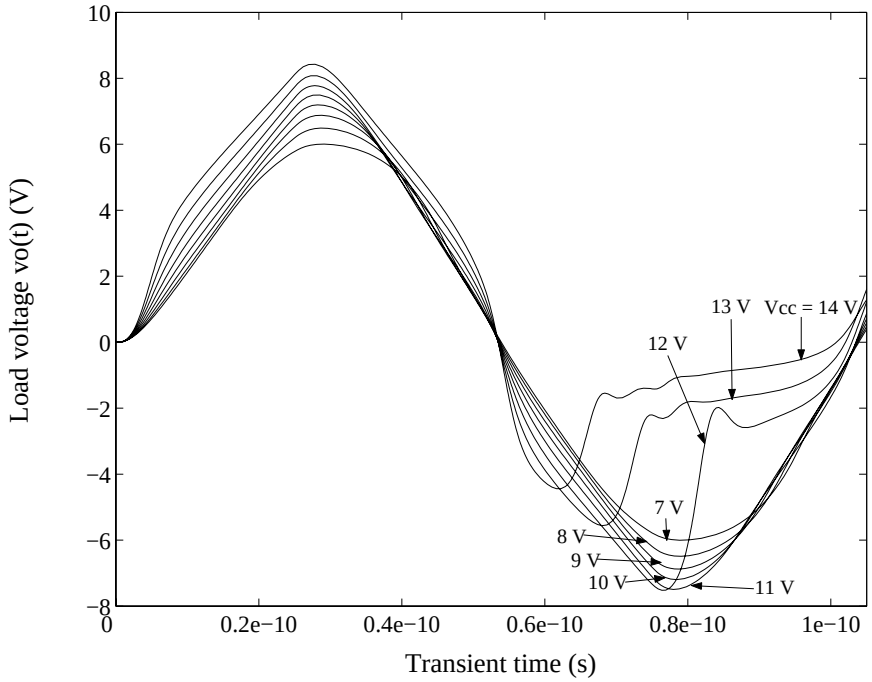

Fig. 4.16 Load voltage $v_o(t)$ in Fig. 4.10 when using two layer PCSS structures with V_{cc} set from 7 V to 14 V.

Table 4.6 shows the important characteristics of the amplifier as a function of V_{cc} for the five cases in Fig. 4.16 for which the output voltage is reasonably triangular and the equations for the triangular approximation can be applied. The third column shows that the half-triangular optical pulses have peak power of 0.48 W and average power of 0.24 W which is four times larger than in Table 4.2 for the single layer PCSS. This is because we doubled both the width and the depth of our single-layer device to form the two-layer device. This results in four times higher illuminated area, which requires four times higher optical average power. Equations (4.13) and (4.16) were used to find the output and input powers of the amplifier. The results are shown in the fourth and fifth columns of Table 4.6, respectively. The results show that the output power of the amplifier with two-layer PCSSs is also approximately four times larger than in the single-layer case. The

V_{CC} (Volts)	V_o(max) (Volts)	P_{opt} (Watts)	P_s (Watts)	P_o (Watts)	Efficiency (η,%)	Gain (db)	PAE (%)
7	6.05	0.24	0.424	0.244	57.6	0.2	1.0
8	6.60	0.24	0.528	0.290	55.0	1.7	9.5
9	7.00	0.24	0.630	0.327	51.9	2.7	13.8
10	7.35	0.24	0.735	0.360	49.0	3.5	16.4
11	7.65	0.24	0.842	0.390	46.4	4.2	17.8

Table 4.6 Characteristics of the OE Class AB push-pull PA using two-layer PCSSs as V_{cc} in Fig. 4.10 is varied from 7 to 11 Volts.

reason for that is that we are able to double the circuit output voltage and according to Equation (4.13), output power is proportional to the output voltage squared. This can be seen by comparing V_{cc} = 5 V in Table 4.2 and V_{cc} = 10 V in Table 4.6. Finally, the sixth column of Table 4.6 shows the efficiency of the amplifier. In the cases of reasonably low signal distortion, i.e., for V_{cc} equals to 7 to 11 V, the efficiency of the circuit is 57.6 to 46.4 %, which is essentially the same as in the one-layer case. Therefore, with two-layer device, we can increase the output power by a factor of 4 without sacrificing circuit efficiency, gain, or PAE.

A similar simulation was conducted with a three-layer PCSS structure. In order to eliminate the series resistance problem, the depth of the device was set to 9 um as discussed in Section 3.3. Fig. 4.17 shows the Mixedmode simulation result of the photocurrent $i_o(t)$ in Fig. 4.3 when using a three-layer intrinsic GaAs PCSS structure. The photocurrents $i_o(t)$ result from a triangular optical pulse train and with the voltage V_{cc} in Fig. 4.3 set in turn to 9 V to 21 V with the increment of 1 V. Here, we eliminate all the voltages below 8 V due to the current limitation which flatters and makes the waveform unusable. With a three-layer PCSS, the bias voltage V_{cc} can be increased to 21 V which

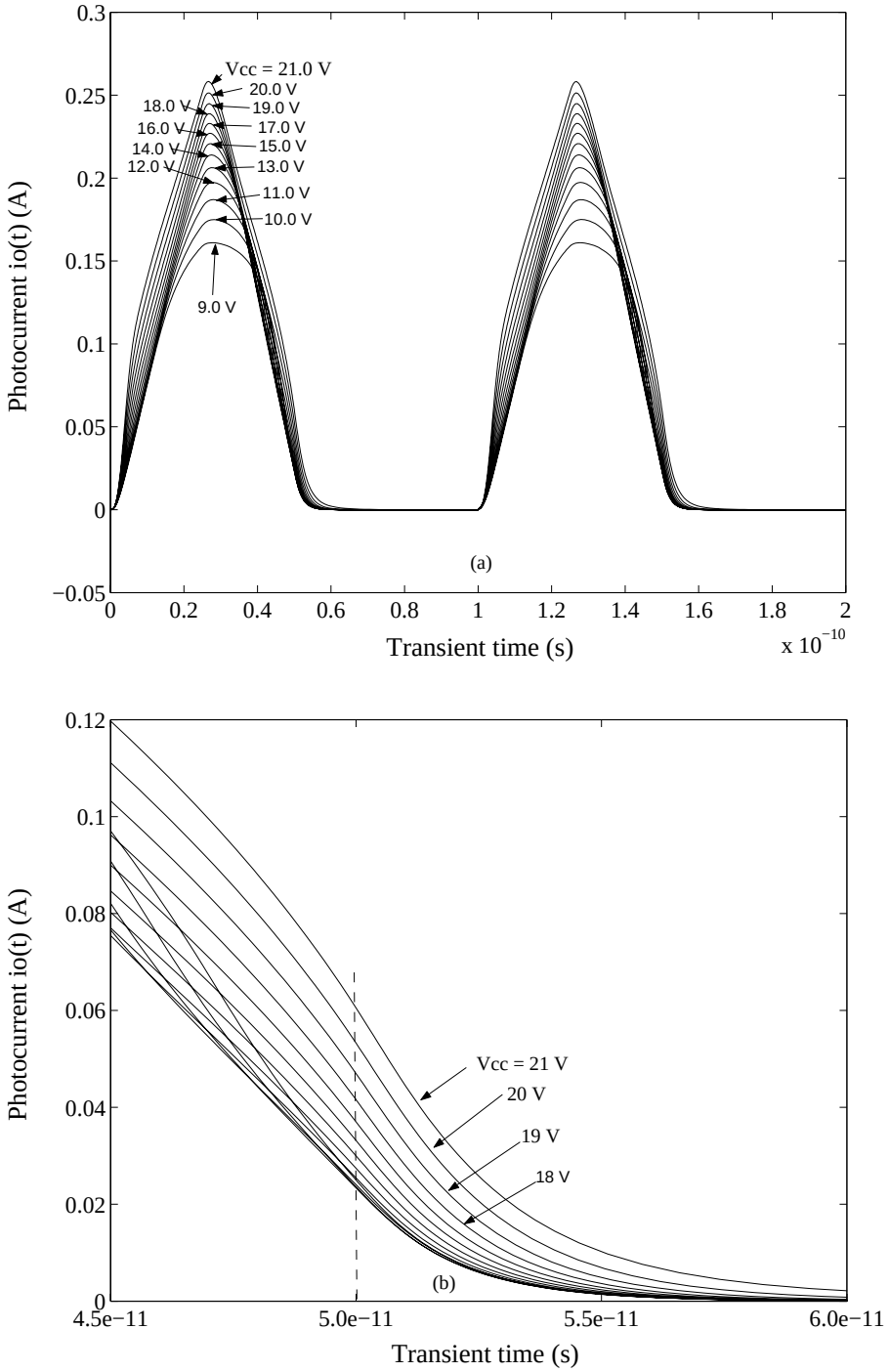

Fig. 4.17 Photocurrent $i_o(t)$ in Fig. 4.3 due to a three-layer intrinsic GaAs PCSS structure: (a) output due to two laser pulses of the type shown in Fig. 4.4, with V_{cc} set to thirteen different values, (b) expansion of the data shown in Fig. 4.17(a) between $4.5*10^{-11}$ and $6.0*10^{-11}$ s.

corresponds to 700 KV/cm breakdown voltage, again showing the agreement with a single layer PCSS. Due to the onset of avalanche, as Fig. 4.1(b) shows, the recovery time of the photocurrent begins to increase significantly beyond the 50.0 ps point required for 10.0 GHz operation at higher bias voltage.

Table 4.7 shows the characteristics of a three-layer PCSS structure as V_{cc} in Fig. 4.17 is varied. The results are similar to those for the single layer and double-layer PCSS structures, shown in Table 4.1 and Table 4.5, respectively. For example, when the E (max) equals 500 KV/cm, as listed in the seventh column for all three cases, the minimum resistance, R_{pc} (min), listed in the third column and the circuit peak efficiency, listed in the sixth column are similar, which again indicates that the multi-layer PCSS can be utilized in our amplifier to obtain higher power.

V_{CC} (Volts)	i_o (max) (Amps)	R_{pc} (min) (Ohms)	v_{pc} (min) (Volts)	v_o (max) (Volts)	v_o (max)/V_{cc}	E (max) (KV/cm)	E (min) (KV/cm)
9	0.161	5.90	0.95	8.05	0.89	300	31.7
10	0.175	7.14	1.25	8.75	0.88	333	41.7
11	0.187	8.82	1.65	9.35	0.85	367	55.0
12	0.197	10.91	2.15	9.85	0.82	400	71.7
13	0.206	13.11	2.70	10.30	0.79	433	90.0
14	0.214	15.42	3.30	10.70	0.76	467	110.0
15	0.221	17.87	3.95	11.05	0.74	500	131.7
16	0.227	20.48	4.65	11.35	0.71	533	155.0
17	0.233	22.96	5.35	11.65	0.69	567	178.3
18	0.239	25.31	6.05	11.95	0.66	600	201.7
19	0.245	27.55	6.75	12.25	0.64	633	225.0
20	0.251	29.68	7.45	12.55	0.63	667	248.3
21	0.258	31.40	8.10	12.90	0.61	700	270.0

Table 4.7 Characteristics of a three-layer PCSS structure as V_{cc} in Fig. 4.3 is varied from 9 V to 21 V.

Figure 4.18 shows the simulation results for the OE Class AB push-pull microwave PA shown in Fig. 4.10 when our three-layer PCSSs are used. Results are shown for the bias voltage V_{cc} set from 11 V to 21 V. For the bias voltage above 17 V, we observe that the load voltages are increasingly distorted because of the avalanche effect.

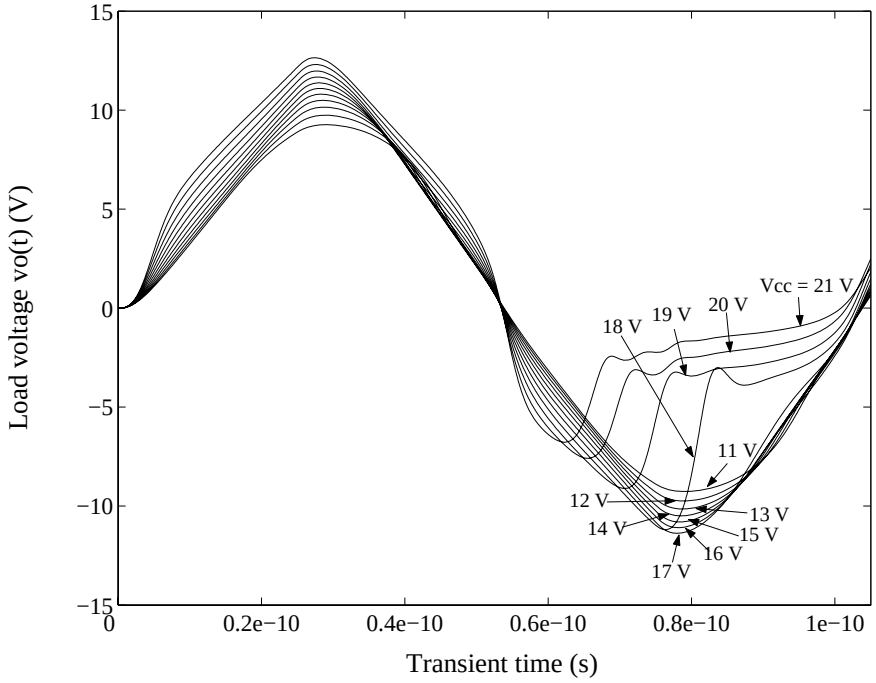

Fig. 4.18 Load voltage $v_o(t)$ in Fig. 4.10 when using three layer PCSS structures with V_{cc} set from 11 V to 21 V.

Table 4.8 shows the important characteristics of the amplifier as a function of V_{cc} for the six cases in Fig. 4.18 for which the output voltage is reasonably triangular and the equations for the triangular approximation can be applied. The third column shows that the peak optical power is now 1.08 W and the average optical power is now 0.54 W because the illumination area of the device is now nine times the single-layer case. As before, equations (4.13) and (4.16) were used to find the output and input powers of the

V_{CC} (Volts)	V_o(max) (Volts)	P_{opt} (Watts)	P_s (Watts)	P_o (Watts)	Efficiency (η,%)	Gain (db)	PAE (%)
11	9.35	0.54	1.029	0.583	56.7	0.7	4.2
12	9.85	0.54	1.182	0.647	54.7	1.6	9.0
13	10.30	0.54	1.339	0.707	52.8	2.3	12.5
14	10.70	0.54	1.498	0.763	51.0	3.0	14.9
15	11.05	0.54	1.658	0.814	49.1	3.6	16.5
16	11.35	0.54	1.816	0.859	47.3	4.0	17.6

Table 4.8 Characteristics of the OE Class AB push-pull PA using three-layer PCSSs as V_{cc} in Fig. 4.10 is varied from 11 to 16 Volts.

amplifier. The results are shown in the fourth and fifth column of Table 4.6, respectively. Since three times more voltage can be applied in the PA circuit using three-layer PCSSs, we are able to obtain approximately nine times more output power than by using single layer PCSSs. In the cases of reasonably low signal distortion, i.e., for V_{cc} = 11 – 16 V, the efficiency of the circuit is 56.7 to 47.3 %, which again is approximately the same with in the one- and two-layer devices.

Our simulations show that the best linearity, efficiency, gain, and PAE always occur for bias fields between 400 KV/cm and 500 KV/cm. Moreover, we can stack layers in the PCSS in order to increase the output power of the circuit. However, there is a limitation to the number of layers, which is the available average optical power of the semiconductor laser. From our research [66], the highest CW semiconductor laser for the wavelength of 850 nm is 3 W. Considering the modulator, the highest average output laser power we can obtain is approximately 1.5 W. When we increase the layer structure to five layers (PCSS width is 0.5 um), for maintaining the same current density inside the PCSS, the depth of the device needs to increase to 15 um. This would increase the illuminated area to 7.5 um^2 keeping the peak optical intensity of $4*10^7$ W/cm^2, means we

would need a peak optical power of 3.0 W or average optical power of 1.5 W. Therefore, we are limited to a maximum of five-layers in our PCSS structure.

Fig. 4.19 shows the five-layer PCSS structure. There are Schottky contacts in six y-z faces at x = 0 um, 0.1 um, 0.2 um, 0.3 um, 0.4 um, and 0.5 um. The depth of the PCSS increases to 15 um in order to maintain minimum resistance and limit the current density of the device. The entire surface is illuminated by 0.85 um optical triangular pulses as usual. Fig. 4.20 shows the Mixedmode simulation results of the output voltage of the amplifier with five-layer PCSSs with bias voltages of 20 V and 25 V, corresponding to 400 KV/cm and 500 KV/cm electric fields, respectively. Table 4.9 shows the important characteristics of the amplifier. For V_{cc} = 20 V and 25 V, the efficiency of the circuit is 54.6 and 48.6 %, which are similar to the single layer, two-layer and three-layer PCSS cases. The gain and PAE results are similar to other cases. However, with the five-layer structure, we are able to increase the circuit average output power to 1.79 W and 2.21 W when the V_{cc} is biased at 20 V and 25 V, respectively.

Fig. 4.20 also shows two perfect triangular waveforms at 10 GHz frequency. The Waveform "A" has the same peak amplitude value as the V_{cc} = 20 V result and Waveform "B" has the same peak amplitude value as the V_{cc} = 25 V result. Comparing the corresponding pair of cases, we see that our amplifier can closely follow the rise-time of the triangular pulse; however, the turn-off time is slightly slower than the fall time of the triangular pulse, although our PCSS can still operate successfully at 10 GHz. The reason for the slow turn-off time is that it still takes time for the photo-generated carriers to sweep-out of the device even with the ballistic transport mechanism. Equation (4.18)

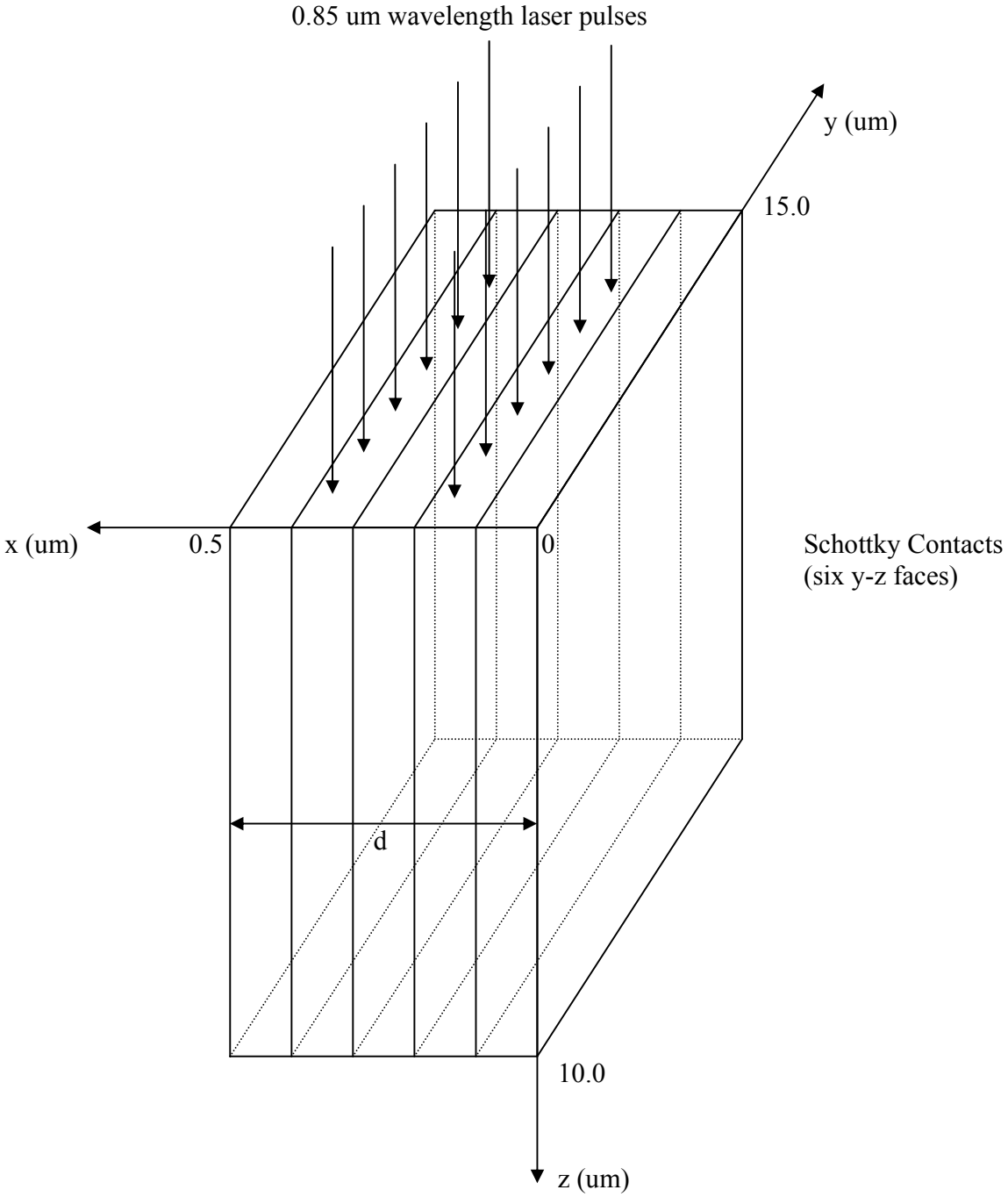

Fig. 4.19 Five-layer GaAs photoconductive semiconductor switch (PCSS). The upper face is uniformly illuminated by 0.85 um wavelength laser pulses.

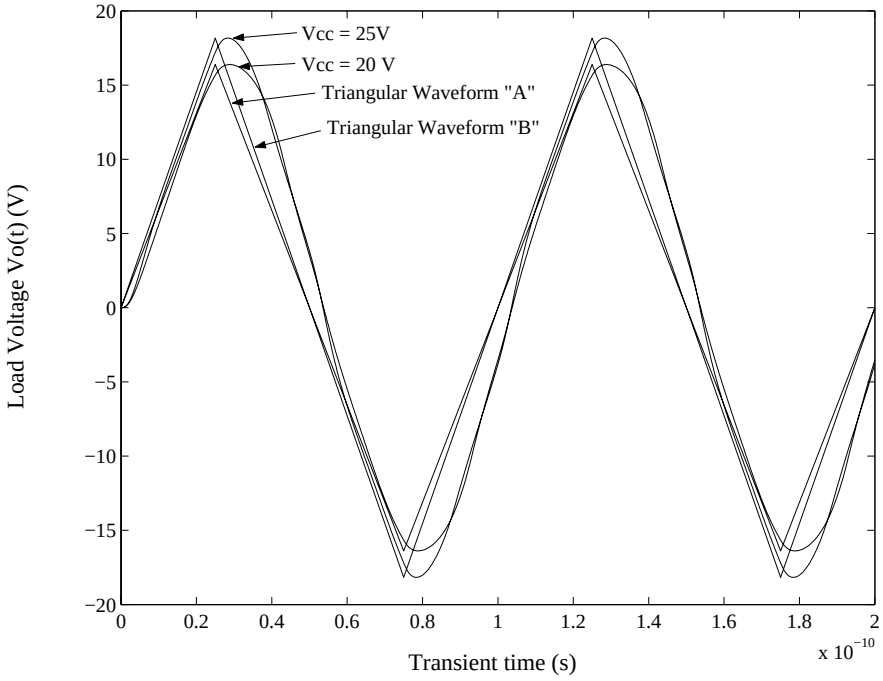

Fig. 4.20 Load voltage $v_o(t)$ in Fig. 4.10 when using five-layer PCSS structures with V_{cc} set to 20 V and 25 V and two perfect triangular waveforms with the frequency of 10 GHz.

was used in order to calculate the total harmonic distortion (THD) of our output waveforms.

$$THD = \sqrt{\frac{V_{rms}^{\ 2} - V_{1,rms}^{\ 2}}{V_{1,rms}^{\ 2}}} \qquad (4.18)$$

V_{CC} (Volts)	V_o(max) (Volts)	P_{opt} (Watts)	P_s (Watts)	P_o (Watts)	Efficiency (η,%)	Gain (db)	PAE (%)	THD (%)
20	16.4	1.5	3.28	1.79	54.6	1.54	8.84	69
25	18.2	1.5	4.55	2.21	48.6	3.37	15.6	60

Table 4.9 Characteristics of the OE Class AB push-pull PA using five-layer PCSSs as V_{cc} in Fig. 4.10 is set to 20 and 25 Volts.

Matlab software was used to find the Fourier series of the two amplifier load voltage waveforms shown in Fig. 4.20. In addition, we also found the Fourier series of the two perfect triangular waveforms. One hundred harmonic components were cal culated. Therefore, V_{rms} and $V_{1,rms}$ for use in equation (4.18) were determined. The ninth column of Table 4.9 shows the THD to be 69 % and 60 % for V_{cc} = 20 V and V_{cc} = 25 V, respectively. Filtering circuit can be used to reduce the THD values.

Chapter 5 Conclusion and Extension

In this chapter, we will first summarize the important contribution of this dissertation. Then, we will discuss the work than can be accomplished in the future in order to improve upon the present results.

5.1 Conclusion

An intrinsic GaAs photoconductive switch that can operate at 10 GHz frequency (X-band) has been designed and analyzed. The key feature of the switch is its narrow (0.1 μm) width in the direction of current flow, which enables rapid removal of photocarriers by sweep-out at carrier velocities greater than the saturated drift velocity. The response of the PCSS to 50 ps wide triangular optical pulses at 10 GHz is limited at low bias voltages by the current limiting behavior of the 50 ohm load resistance and at sufficiently large bias voltages where the breakdown electric field of the semiconductor is exceeded and avalanche begins, thus increasing the switch turn-off time. Thus, an optimum, intermediate value of bias voltage exists where efficiency and distortion are both reasonable and acceptable.

By using our novel PCSSs in a new OE Class AB PA, we have obtained simulated efficiency value of 50 % at 10 GHz. The output signal is reasonably undistorted with an average power between 50 and 85 mW. In addition, by using optical illumination, input matching networks, which are required when using electrical RF input signals, are not necessary, thereby reducing the complexity of the new amplifier. Another advantage of

using our new EO PA is the isolation of the input optical circuit from the main PA circuit, which allows us to stack several PCSS devices together to form an equivalent multi-layer PCSS. This should make it possible to use higher V_{cc} values, which would lead to increased output power. Simulations showed that the OE Class AB PA with five-layer PCSS devices can produce an average microwave output power of 2.2 W at 10 GHz while maintaining a circuit efficiency around 50 %. The observed efficiencies of the new optoelectronic amplifier represent an improvement over currently available, electronically driven X-band microwave amplifiers. This result and the relative simplicity of the amplifier should contribute to the development of compact, light-weight, mobile phased array radar systems.

5.2 Extension

More parametric simulation on PCSS device heights will be studied. We will make the on-state resistance in the PCSS more uniformly distributed by reducing the PCSS height to from 10 um to 2 um. In addition, in order to test the accuracy of PCSS/OE amplifier simulations, intrinsic GaAs PCSS devices need to be fabricated and tested, including multi-layer structures. Fabricating the Schottky contacts may be a challenge. Furthermore, in order to test the lock-on theory we proposed in Section 3.1.2, devices made with semi-insulating GaAs PCSS need to be fabricated and tested. Next, we will simulate our OE Class AB PA with sinusoidal optical waveform instead of the triangular optical pulse. Then, our OE Class AB PA must be built and tested. For improve the THD value we showed in Section 4.5, a filter will be required at the output

of the PA. Finally, the ultimate goal of this project is to produce a compact, fully integrated MMIC power amplifier circuit at X-band operation that can be utilized to produce more compact and lighter microwave systems.

Reference

[1] William C. Nunnally, etc., "Advanced Radars and Electro-optical Sensors (ARES)", Technical and Management Proposal, University of Missouri-Columbia, May, 2001.

[2] David M. Pozar, *Microwave and RF Design of Wireless Systems*, John Wiley & Sons Inc., New York, 2001.

[3] Frederick H. Raab, P. Asbeck, S. Cripps, P.B. Kenington, Z.B. Popovic, N. Pothecary, J.F. Sevic, and N.O. Sokal, "Power Amplifiers and Transmitters for RF and Microwave," *IEEE Transactions on Microwave Theory and Techniques*, Vol. 50, No. 3, MARCH 2002, PP. 814-826.

[4] H. Krauss, C. Bostian, F. Raab, *Solid State Engineering*, John Wiley & Sons, Canada, 1980.

[5] Mihai Albulet, *RF Power Amplifiers*, Noble Publishing, Atlanta GA, 2001.

[6] Zhenqiang Ma, Saeed Mohammadi, Liang-Hung Lu, Pallab Bhattacharya, Linda P. B. Katehi, Samuel A. Alterovitz, and George E. Ponchak, "An X-band High-Power Amplifier Using SiGe/Si HBT and Lumped Passive Components", *IEEE Microwave and Wireless Components Letters*, Vol. 11, No. 7, July 2001

[7] Mark N. Horenstein, *Microelectronic Circuits & Devices*, Prentice-Hall International Editions, N.J., 1990.

[8] Pang-Cheng Hsu, Cam Nguyen, and Mark Kintis, "Uniplanar Broad-Band Push-Pull FET Amplifiers", *IEEE Transactions on Microwave Theory and Techniques,* Vol. 45, No. 12, December 1997.

[9] V. Paidi, S. Xie, R. Coffie, B. Moran, S. Heikman, S. Keller, A. Chini, S.P. DenBaars, U.K. Mishra, S. Long, and M.J.W. Rodwell, "High Linearlty and High Efficiency of Class B Power Amplifiers in GaN HEMT Technology", *IEEE Transactions on Microwave Theory and Techniques,* Vol. 51, No. 2, February 2003.

[10] V. Radisic, S.T. Chew, Y. Qian, and T. Itoh, "High Efficiency Power Amplifier Integrated with Antenna", *IEEE Microwave and Guide Wave Letters*, Vol. 7, No. 2, February 1997.

[11] W.R. Deal, V. Radisic, Y. Qian, and T. Itoh, "Novel Push-Pull Integrated Antenna Transmitter Front-End", *IEEE Microwave and Guide Wave Letters*, Vol. 8, No. 11, November 1998.

[12] W.R. Deal, V. Radisic, Y. Qian, and T. Itoh, "Integrated-Antenna Push-Pull Power Amplifiers", *IEEE Transactions on Microwave Theory and Techniques,* Vol. 47, No. 8, August 1999.

[13] C.Y. Hang, W.R. Deal, Y. Qian, and T. Itoh, "High-Efficiency Push-Pull Power Amplifier Integrated with Quasi-Yagi Antenna", *IEEE Transactions on Microwave Theory and Techniques,* Vol. 49, No. 6, June 2001.

[14] Wei Wang, and Y.P. Zhang, "0.18-um CMOS Push-Pull Power Amplifier with Antenna in IC Package", *IEEE Microwave and Wireless Components Letters*, Vol. 14, No. 1, January 2004.

[15] Ravi Gupta, Brian M. Ballweber, and David J. Allstot, "Design and Optimization of CMOS RF Power Amplifiers", *IEEE Journal of Solid-State Circuits*, Vol. 36, No, 2, February 2001.

[16] Afonso Coelho Nunes, Maria Joao do Rosario, and J.C. Freire, "A Microstrip Matching Network for Class C Power Amplifiers Optimization", *Microwave Conference and Exhibition, 27th European,* Vol. 2, PP. 761-766, September 1997.

[17] Sayed-Amr El-Hamamsy, "Design of High-Efficiency RF Class-D Power Amplifier", *IEEE Transaction on Power Electronics*, Vol. 9, No. 3, May 1994.

[18] K. Nandhasri, J. Ngarmnil, and K. Moolpho, "A 2.8V RWDM BTL Class-D Power Amplifier using an FGMOS Comparator", *IEEE International Symposium on Circuits and Systems (ISCAS)*, Vol. 5, PP. 26-29, May 2002.

[19] Hidenori Kobayashi, Jeff Hinrichs, and Pwter M. Asbeck, "Current Mode Class-D Power Amplifiers for High Efficiency RF Applications", *IEEE Transactions on Microwave Theory and Techniques,* Vol. 49, No. 12, December 2001.

[20] Hidenori Kobayashi, Jeff Hinrichs, and Pwter M. Asbeck, "Current Mode Class-D Power Amplifiers for High Efficiency RF Applications", *Microwave Symposium Digest, IEEE MTT-S International*, Vol. 2, PP. 20-25, May 2001.

[21] Nathan O. Sokal, "Class E High-Efficiency Power Amplifiers, from HF to Microwave", *Microwave Symposium Digest, IEEE MTT-S International*, Vol. 2,

PP. 1109-1112, June 2001.

[22] Manoja D. Weiss and Zoya Popovic, "A 10 GHz High-Efficiency Active Antenna", *Microwave Symposium Digest, IEEE MTT-S International*, Vol. 2, PP. 13-19, June 1999.

[23] R. Tayrani, "A Monolithic X-band Class-E Power Amplifier", *Gallium Arsenide Integrated Circuit (GaAs IC) Symposium, 23rd Annual Technical Digest*, PP. 205-208, October 2001.

[24] Zoya Popovic, Srdjan Pajic, Narisi Wang, and Patrick Bell, "Efficiency X-band Switch-Mode Microwave Power Amplifiers", *Gallium Arsenide Integrated Circuit (GaAs IC) Symposium, 23rd Annual Technical Digest*, PP. 125-128, November 2003.

[25] Vladimir Sokolov, Ralph E. Williams, and Don W. Shaw, "X-band Monolithic GaAs Push-Pull Amplifiers", *Solid-State Circuits Conference, Digest of Technical Papers, 1979 IEEE International*, Vol. XXII , PP. 118-119, February 1979.

[26] I.M. Abolduyev, A.M. Zubkov, and V.M. Minnebaev, "X-Band Power Amplifier for Active Phased-Array Antennas", *ICSC '98, the Third International Conference on Satellite Communications*, Vol. 1, PP. 170-171, September. 1998

[27] C.Y. Chang and Francis Kai, *GaAs High Speed Devices*, John Wiley & Sons, N.Y., 1994.

[28] Fazal Ali and Aditya Gupta, *HEMTs & HBTs: Devices, Fabrication, and Circuits*, Artech House, Boston, 1991.

[29] Alvaro A. De Salles, and Murilo A. Romero, "AlGaAs/GaAs HEMT's Under Optical Illumination", *IEEE Transaction on Microwave Theory and Techniques*, Vol. 39, No. 12, pp. 2010-2017, December 1991.

[30] Rainee N. Simons, "Microwave Performance of an Optically Controlled AlGaAs/GaAs High Electron Mobility Transistor and GaAs MESFET", *IEEE Transactions on Microwave Theory and Techniques*, Vol. MTT-35, No. 12, pp. 1444-1455, December 1987.

[31] Alwyn J. Seeds, and Alvaro A. De Salles, "Optical Control of Microwave Semiconductor Devices", *IEEE Transactions on Microwave Theory and Techniques*, Vol. 38, No. 5, pp. 577-585, May 1990.

[32] Rainee N. Simons, and Kul B. Bhasin, "Analysis of Optically Controlled Microwave/Millimeter-Wave Device Structures", *IEEE Transactions on*

Microwave Theory and Techniques, Vol. MTT-34, No. 12, pp. 1349-1355, December 1986.

[33] Murilo A. Romero, M. A. G. Martinez, and Peter R. Herczfeld, "An Analytical Model for the Photodetection Mechanisms in High-Electron Mobility Transistors", *IEEE Transactions on Microwave Theory and Techniques*, Vol. 44, No. 12, pp. 2279-2287, December 1996.

[34] Jian Lu, R. Surridge, G. Pakulski, H. Van Driel, and J. M. Xu, "Studies of High Speed Metal-Semiconductor-Metal Photodetector with a GaAs/AlGaAs/GaAs Heterostructure", *IEEE Transactions on Electron Devices,* Vol. 40, NO. 6, pp. 1087-1092, June 1993.

[35] Ali F. Salem, Arlynn W. Smith, and Kevin F. Brennan, "Theoretical Study of the Effect of an AlGaAs Double Heterostructure on Metal-Semiconductor-Metal Photodetector Performance", *IEEE Transactions on Electron Devices,* Vol. 41, NO. 7, pp. 1112-119, June 1993.

[36] W.C. Nunnally and R.B. Hammond, "80-MW Photoconductive Power switch", *Applied Phsics Letter,* Vol. 44, No. 10, pp. 980-982, May 1984.

[37] Fred J. Zutavern, Guillermo M. Loubriel, M.W. O'Malley, L.P. Schanwald, and D.L. McLaughlin, "Recovery of High-Field GaAs Photoconductive Swmicinductor Switches", *IEEE Transaction on Electron Devices*, Vol. 38, No. 4, pp. 696-700 April, 1991.

[38] Arye Rosen and Fred Zutavern, *High-Power Optically Activated Solid-State Switches*, Artech House, Boston, 1993.

[39] W.C. Nunnally, "High-Power Microwave Generation Using Optically Activated Semiconductor Switches", *IEEE Transaction on Electron Devices*, Vol. 37, No. 12, pp. 2439-2448, December, 1990.

[40] N.E. Islam, E. Schamiloglu, C.B. Fleddermann, J.S.H. Schoenberg, and R.P. Joshi, "Improved Hold-off Characteristics of Gallium Arsenide Photoconductive Switches Used in High Power Applications", *Pulse Power Conference*, *Digest of Technical Papers, 12th IEEE International*, Vol. 1, pp. 316-319, June 1999.

[41] John A. Gaudet etc., "Progress in Gallium Arsenide Photoconductive Switch Research for High Power Applications", *Power Modulator System, 2002 High-Voltage Workshop, Conference Record of the 25th international*, pp. 699-702, July 2002.

[42] G.M. Loubriel, F.J. Zutavern, W.D. Helgeson, D.L. McLaughlin, M.W. O'Mally, and T. Burke, "Physics and Applications of the Lock-On Effect", *Pulse Power*

Conference, *1991 Digest of Technical Papers, 8th IEEE International*, pp. 33-36, June 1991.

[43] M.A. Gunderson, J.H. Hur, and H. Zhao, "Lock-On Effect in Pulsed-Power Semiconductor Switches", *Journal of Applied Physics*, Vol. 71, No. 6, pp. 3036-3038, March 1991.

[44] Phillip J. Stout and Mark J. Kushner, "Modeling of High Power Semiconductor Switches Operated in the nonlinear mode", *Journal of Applied Physics*, Vol. 79, No. 4, pp. 2084-2090, February 1996.

[45] M.D. Pocha, R.L. Druce, M.J. Wilson, and W.W. Hofer, "Avalanche Photoconductive Switching", *Pulse Power Conference*, *Digest of Technical Papers, 7th IEEE International*, Vol. 1, pp. 866-868, June 1989.

[46] F J. Zutavern, G.M. Loubriel, B.B. McKenzie, M.W. O'Malley, W.D. Helgeson, and D. L. McLaughlin, "High Gain Photoconductive Semiconductor Switching", *Pulse Power Conference*, *Digest of Technical Papers, 8th IEEE International*, Vol. 1, pp. 23-28, June 1991.

[47] F J. Zutavern, G.M. Loubriel, B.B. McKenzie, M.W. O'Malley, R.A. Hamil, L.P. Schanwald, and H.P. Hjalmarson, "Photoconductive Semiconductor Switch (PCSS) Recovery", *Pulse Power Conference*, *Digest of Technical Papers, 7th IEEE International*, Vol. 1, pp. 412-417, June 1989.

[48] Michael D. Pocha and Robert L. Druce, "35-KV GaAs Subnanosecond Photoconductive Switches", *IEEE Transaction on Electron Devices*, Vol. 37, No. 12, pp. 2486-2492, December, 1990.

[49] F J. Zutavern, G.M. Loubriel, B.B. McKenzie, M.W. O'Malley, W.D. Helgeson, D. L. McLaughlin, and G.J. Denison, "Characteristics of Current Filamentation in High Gain Photoconductive Semiconductor Switching", *Power Modulator System, Conference Record of the 20th international*, pp. 305-311, June 1992.

[50] K. Kambour, Samsoo Kang, Charles W. Myles, and Harold P. Hjalmarson, "Steady-State Properties of Lock-On Current Filaments in GaAs", *IEEE Transaction on Plasma Science*, Vol. 28, No. 5, pp. 1497-1499, October 2000.

[51] E. Schamiloglu, N.E. Islam, C.B. Fleddermann, B. Shipley, R.P. Joshi, and L. Zheng, "Simulation, Modeling, and Experimental Studies of High-Gain Gallium Arsenide Photoconductive Switches for Ultra-Wideband applications", *Ultra-Wideband Short Pulse Electromagnetics 4*, pp. 221-228, June 1998.

[52] M.S. Mazzola, K.H. Schoenbach, V.K. Lakdawala, and R. Germer, "GaAs Photoconductive Closing Switches with High Dark Resistance and Microsecond

Conductivity Decay", *Applied Physics Letter*, Vol. 54, No. 8, pp. 742-744, February 1989.

[53] Naz E. Islam, Edl Schamiloglu, Jon H. Schoenberg, and R.P. Joshi, "Compensation Mechanisms and the Response of High resistivity GaAs Photoconductive Switches During High-Power Applications", *IEEE Transactions on Plasma Science*, Vol. 28, No. 5, pp. 1512-1519, October 2000.

[54] J.S. Blakemore, L. Sargent, and R-S. Tang, "Assessment of the Ionized EL2 Fraction in Semi-insulating GaAs", Apply Physics Letter, Vol. 54, No. 21, pp. 2106-2108, May 1989.

[55] Richard H. Bube, *Photoelectronic Properties of Semiconductors*, Cambridge University Press, Cambridge, UK, 1992.

[56] H.P. Hjalmarson, G.M. Loubriel, F.J. Zutavern, D.R. Wake, Samsoo Kang, K. Kambour, and Charles W. Myles, "A Collective Impact Ionization Theory of Lock-On", *Pulse Power Conference*, *Digest of Technical Papers, 12th IEEE International*, Vol. 1, pp. 299-302, June 1999.

[57] K. Kambour, H.P. Hjalmarson, and Charles W. Myles, "A Collective Theory of Lock-On in Photoconductive Semiconductor Switches", *Pulse Power Conference*, *Digest of Technical Papers, 14th IEEE International*, Vol. 1, pp. 345-348, June 2003.

[58] K.E. Kambour, H.P. Hjalmarson, and Charles W. Myles, "Theory of Optically-Triggered Electrical Breakdown of Semiconductors", *Conference on Electrical Insulation and Dielectric Phenomena, Annual Report*, pp. 345-348, October 2003.

[59] Kun-Chyi Huang, "Electro-Optical Class AB Microwave Amplifier Test Waveform", *Master Project Report*, University of Missouri-Columbia, August 2004.

[60] Donald A. Neamen, *Semiconductor Physics & Devices: Basic Principles*, 2nd Edition, Irwin, The McGrae-Hill Companies, INC., 1997.

[61] Silvaco International, 4701 Patric Henry Drive, Santa Clara, CA, www.silvaco.com.

[62] Silvaco International, *ATLAS User'Manual: Device Simulation Software*, Volume I & II, Santa Clara, CA, 2000.

[63] ADTECH Photonics, Inc., 850 nm Laser Diodes, www.adtechphotonics.com/html/850_nm_laser_diodes.html.

[64] Daniel W. Hart, *Introduction to Power Electronics*, Prentice Hall Inc., New Jersey, 1997.

[65] Leif A. Johansson, Yuliya A. Akulova, Greg A. Fish, and Larry A. Coldren, "Chirp-Controlled Tandem Electroabsorption Modulator Integrated with an SOA and a Sampled-Grating DBR laser", *The 16th Annual Meeting of the IEEE Lasers and Electro-Optics Society,* Vol. 1, pp. 433-434, October 2003.

[66] JDS Uniphase, 430 N. McCarthy Blvd., Milpitas, CA 95035, USA, www.jdsu.com.

VITA

Chih-Jung Jerome Huang was born in Taipei, the capital city of Taiwan, on July 30, 1974. After attending public schools in Taipei, he received his junior college diploma in the field of Electronic Engineering from the Kuang-Wu Junior College of Technology in 1994. After graduating from the junior college, he attended the Air Force serving as the Sergeant position in Hualien, Taiwan. After two-year military service, he came to United State of America and attended the University of Missouri in Columbia to continue his study in Electrical and Computer Engineering. He received his B.S. and M.S. degrees in 1999 and 2001, respectively. He earned his Ph.D. degree in August 2006.